UPC

RSLab

Atmosphere characterisation with SAR interferometry

MERIT, M.Sc. Dissertation

Author:
Gorka Moyano Sánchez

Supervisor:
Paco López Dekker

2008-2009

It is a far, far better thing that I do, than I have ever done;
it is a far, far better rest that I go to, than I have ever known.

Final sentence of *A Tale of Two Cities*

Acknowledgements

I am going to talk about people who I have spent the last year with, the year that has been devoted to this project. In general, it has been a good year.

First of all, I would like to thank everyone that have helped me with this project. My project advisor, Paco, the responsible, among other things, that this is the only section of the project where I have used the word *I* (or even *we*!). It is expected that the other things are more important. Dani, always kind when I wanted him to do some interferograms. After Paco, he is the person who has helped me the most, the number two on board. All the other people who have done smaller contributions (though equally important), who this margin is too narrow to contain. At least I will always remember them.

My family, who must be using a dictionary or a translator to know what I am saying to them, well, here it goes: if you want to know what the project is about, look at the photos. I would like to mention the newborn baby, Lara, who is the daughter of the sister of the brother-in-law... To my sister (English my), this conversation is being recorded, for your security: three eights? or three,eight?

To my friends from here and from there. A special mention to Lograr, they are the only who may know how I feel finishing the project. Among them, Mondy and Xavi, it has been an entertaining year with them. I do not want to forget the D3 people.

Last but not least, Maria. I do not know what to say that can surprise you. I will think about it tonight and tomorrow I will tell you.

Contents

List of Figures

8

9

List of Tables

Chapter 1

Introduction

1.1 Current situation of SAR remote sensing

Remote sensing is the group of techniques which provides the means to acquire and monitorise information of the land, objects or phenomena. Remote imaging devices do not have the necessity for being located where the object is, but they are mounted on, for instance, a plane or a satellite.

There are two types of remote sensing systems: passive systems and active systems. Passive sensors detect natural radiation emitted or reflected by the observed area. Examples of passive remote sensors include film photography and radiometers. On the other hand, active sensors emit energy with the objective of obtaining information of objects and pieces of land. Imaging radar (RAdio Detection And Ranging) is an example of active remote sensing and is an important technique for observing the Earth's surface.

Radar systems can operate either day or night because they have their own energy source. They transmit a microwave signal towards a scene, after this they receive the portion of the transmitted energy backscattered from the scene. Finally they study the strength (detection) and the time delay (ranging) of the returned signals.

A SAR, Synthetic Aperture Radar, is a coherent radar system whose processing algorithm uses the amplitude and phase of the received signals over successive pulses to generate an image with a high resolution, a SLC.

SAR interferometry is based on the observation of a scene from two points of view slightly different so as to obtain topographic information of the scene, similar to how human eyes work when getting information of depth. SAR differential in-

terferometry systems use SLC images to obtain data of the deformation movement of the surface occurred within the time covered by the images.

Remote sensing sensors can be mounted on various platforms. Satellites have several unique characteristics, which make them very useful for observing the Earth's surface. Sensors onboard satellites normally can see a much larger area of the surface than a sensor onboard an aircraft. Also, since they are continually orbiting the Earth, it is relatively easy to collect imagery on a systematic and repetitive basis in order to monitor changes over time.

A SLC image, acquired from a SAR system on a satellite, contains information on the path length between the radar antenna and the resolution cells on the surface. Effective path length variations are caused by radar signal delay variability within the imaged area, due to the heterogeneous distribution of refractivity. The refractivity directly relates the propagation velocity with the velocity of light in vacuum, and is characterised by water vapour, temperature, pressure or liquid water in the atmosphere. SAR interferograms observe atmosphere induced distortion, but it has typically been treated as noise.

1.2   Purposes of this project

The contribution of the atmosphere in SAR interferometry is not completely known. Therefore, the goal of the project is to characterise the atmosphere, i.e., to study the way it relates to interferograms. The analysis of the atmospheric parameters that have an influence on interferometry will cause a better understanding of the atmosphere.

One of the objectives is to determine the relationship between interferograms and the refractivity calculated on the Earth's surface, to evaluate whether variations or changes of refractivity involve a change in the interferograms.

This work also deals with the analysis of the atmospheric distance of correlation. This distance indicates the maximum separation between two correlated points of the atmosphere. SAR differential interferometry uses this parameter to extract the component of phase due to the atmosphere, so the calculation of velocities of deformation of the land is better.

1.3   Structure of this document

This document consist of 6 chapters. The contents of each chapter are given next.

Chapter 1 is this introduction. Chapter 2 describes the atmosphere, its composition and layers, and the atmospheric parameters that affects interferometry. Chapter 3 explains the theory of SAR interferometry, and the process followed to generate interferograms. Also, it gives the description of the atmospheric component of the interferometric phase, and how it is isolated.

Chapter 4 elaborates on the algorithms designed for this project. They will obtain the results: the comparison between refractivity and the interferometric phase, and the calculation of the atmospheric distance of correlation. Chapter 5 presents and discusses the experimental results.

Chapter 6 extracts the conclusions of the work and presents the future research lines.

Chapter 2

Theory of the Earth's atmosphere

2.1 Description

The Earth is surrounded by a layer of air, a mixture of gases, called atmosphere. It, together with the Sun's energy and the Earth's magnetic fields, supports life on the planet. The atmosphere absorbs ultraviolet solar radiation, warms the surface by retaining the heat, recycles water and other chemicals and reduces temperature extremes between day and night.

The boundary of the atmosphere is not specific, but it becomes thinner and thinner and fades into outer space. In practice, the Kármán line, at 100 km, is commonly used to define the boundary, since this is the point where the atmosphere becomes too thin for aeronautical purposes.

Atmospheric circulation (the large-scale movement of air), with ocean circulation, deals with the distribution of heat on the Earth's surface.

2.2 Composition

Atmospheric gases are divided into constant components, whose amounts do not change over time and position, and variable components, whose proportions change over time and position. The main constant components are nitrogen (N_2), 78.08 %, oxygen (O_2), 20.95 %, and argon (Ar), 0.93 %, whereas the principal variable components are carbon dioxide (CO_2), 0.038 % and water vapour (H_2O), varying
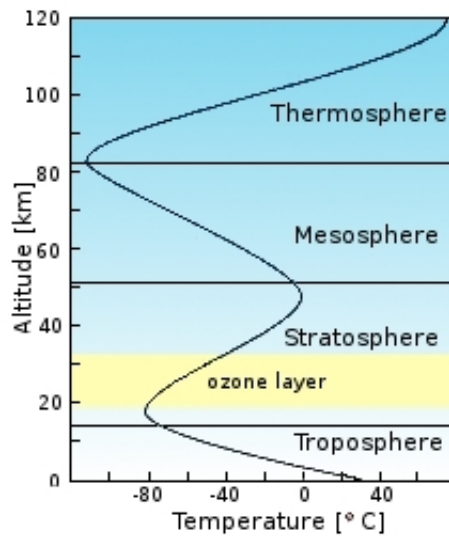
Figure 2.1: Atmospheric layers and the variation of temperature in each layer. In the troposphere and the mesosphere, temperature decreases with increasing height, while in the stratosphere and in the thermosphere, it increases with height.

from 0 to 4 %, one of the most variable atmospheric components.

2.3 Temperature and layers

The atmosphere is not uniform, it consists of five different layers, identified according to the variations temperature, chemical composition, movement and density. Figure 2.1 illustrates the the change of temperature with increasing height. Ordered highest to lowest, the layers and sublayers are:

1. Exosphere: It is the outermost layer, from 640 km up to 1000 km. Low orbit satellites are usually located in the exosphere.

   - Exobase: Also known as the critical level of escape. It is the lower boundary of the exosphere, where atmospheric pressure and temperature are very low.

2. Thermosphere: From 80-85 km to over 640 km, temperature increases with altitude, due to the Sun's energy. The temperature of this layer can rise to 1700°C.

   - Ionosphere: It can be physically characterised by the ability of external sources (mainly the solar ultraviolet radiation and energetic electrons of

solar and magnetospheric origin) to "knock-off" electrons from atoms, therefore creating free electrons that are not bound to their remaining ions. This part of the atmosphere extends from 50 to 1000 km and commonly overlaps both the exosphere and the thermosphere. It plays an important part in atmospheric electricity and makes up the inner edge of the magnetosphere. Due to its charged particles, it has an influence on radio propagation on the Earth.

- Thermopause: The boundary above the thermosphere, it can vary in height from 500-1000 km.

3. Mesosphere: It stretches from about 50 km to 80-85 km. Temperature decreases as height increases. The chemicals are in an excited stated, as they absorb the Sun's energy

- Mesopause: The boundary between the thermosphere and the mesosphere. It records the lower temperatures on Earth, with a minimum of -100℃.

4. Stratosphere: From 7-17 km to about 50 km, temperature increases with height. The stratosphere is dry, so cloud formations is almost nonexistent apart from noctilucent and polar stratospheric clouds. The stratosphere contains the ozone layer.

- Stratopause: The boundary between the mesosphere and the stratosphere, typically from 50 to 55 km.
- Ozone Layer: It is the region from about 10 to 50 km above the surface. It is considered as a layer of the atmosphere in itself, despite being part of the stratosphere. Their physical and chemical composition are far different. The process of the creation of ozone (O_3) in the stratosphere is the following: ultraviolet light hits oxygen molecules (O_2, two oxygen atoms), splitting them into individual oxygen atoms; the atomic oxygen then combines with unbroken O_2 to create O_3. When ultraviolet light strikes ozone, which is unstable, it splits into a molecule of O_2 and an atom of oxygen. It is a continuous process called the ozone-oxygen cycle.

  About 90 % of the ozone in the Earth's atmosphere is in the stratosphere. The concentrations of ozone are greatest in the lower region of the stratosphere, about 15 and 35 km, where they range from around 2 to 8 parts per million. The thickness of the layer varies seasonally and geographically.

5. Troposphere: It is the lowest region of the atmosphere. Troposphere begins at the surface and stretches to between 7 km (at the poles) and 17 km (at the equator), with variations due to the influence of weather. Almost all weather in the atmosphere is in this layer. About the 80 % of the total mass

of the atmosphere is in the troposphere, and the 50 % below 5.6 km. The mean temperature of the atmosphere at the Earth's surface is 15°C, and it decreases as altitude increases.

- Tropopause: The boundary between the stratosphere and troposphere. The temperature does not change with the height in the tropopause.

- Planetary boundary layer (PBL): It is the lowest part of the troposphere, from the surface to 1-2 km, and its behaviour and properties are directly influenced by its contact with the Earth's surface. The thickness of the PBL is not constant: during the day and with warm climate conditions the PBL tends to be thicker, whereas at night and with cool climate conditions it tends to be lower in thickness. In this region, physical magnitudes such as temperature or humidity, display quick fluctuations, and vertical mixing is strong.

2.4   Pressure, density and mass

The pressure of a point in the atmosphere directly relates to the total weight of the air above the point. Atmospheric pressure changes with time and position, since the weight of air above the surface changes with time and position.

At sea level, the mean atmospheric pressure is 1 atmosphere (atm) or 101.3 kPa, while the mean value at the Earth's surface is 98.98 kPa, 2.29 % below the value at sea level. Pressure decreases with increasing altitude, approximately in an exponential way.

The atmospheric density at sea level is around 1.2 kg/m^3. Density decreases as the altitude increases.

The mean value of the atmospheric mass is $5.1480 \cdot 10^{18}$ kg, 1/1200000 the mass of Earth. The 50 % of the atmospheric mass is within 6 km of the surface, and the 75 % 11 km of the surface.

2.5   Opacity

Earth receives Sun's radiation, and it also emits radiation back into space. The atmosphere can filter out radiation, depending on its wavelength, from coming in or going out, such as in the cases, for instance, of the greenhouse effect or the absorption of the ultraviolet radiation by the ozone layer. Figure 2.2 shows the atmosphere from space; elastic or Rayleigh scattering of the sunlight causes the

Figure 2.2: Earth's atmosphere from space. The blue color of the atmosphere is due to Rayleigh scattering. The scattering of shorter (blue) wavelengths of light is easier than longer (red) wavelengths.

blue color of the atmosphere. The most important effects of the atmosphere related to the opacity are scattering, absorption and emission. The greenhouse effect is directly connected to this absorption and emission effects.

2.5.1 Scattering

Photons of light passing through the Earth's atmosphere interact with the atmosphere through scattering. Direct radiation is light that does not interact with the atmosphere, so that it arrives directly to the surface. On the other hand, indirect radiation is light scattered in the atmosphere.

2.5.2 Absorption

Distinct molecules of the atmosphere absorb different wavelengths of electromagnetic radiation. The combination of the absorption spectra of the gases in the atmosphere leads to windows of transmission, or low opacity, which allow the transmission of the bands of radiation corresponding to the bands of the windows. Light that humans can see, the visible spectrum, pass through the optical window, from around 300 nm to around 700 nm.

2.5.3 Emission

Emission of radiation by an object is the opposite term of absorption. The wavelength of emission depends on the black body emission curves of the object, described by the Planck's law, therefore on its temperature. Objects with a high temperature emit radiation with more intensity, but with shorter wavelengths, while objects with a low temperature emit radiation with less intensity, but with longer wavelengths. For instance, the Sun is approximately 5730°C, and its radiation peak is around 500 nm; the atmosphere, due to its temperature, emits infrared radiation.

2.6 Refractivity

The refractivity of air, $N(x, y, z, t)$, is a dimensionless measure that indicates how different is the velocity of propagation in the atmosphere from the velocity of light in vacuum. It is useful when both velocities are very much similar, as it is the case. It is defined as

$$N = 10^6(n - 1), \tag{2.1}$$

where n is the refractive index of the medium, $n = \frac{c}{v_p}$. In the equation of n, c the velocity of light in vacuum and v_p the velocity of propagation in the medium. Thus, N is the difference between the refractive index of the medium and that of vacuum, which is 1. This difference is expected to be very small, so N will consider the sixth decimal of this difference. A refractivity increase leads to a decreases in propagation velocity.

The refractivity, more exactly the integrated refractivity along the path, is directly related to the delay and phase in interferograms [1] [2] [3], explained in Section 3.4.5, and this relationship is the base of this project. The distribution of N is not homogeneous, as it depends on typical atmospheric parameters whose distribution is not homogeneous.

Apart from (2.1), the value of refractivity of a point in the atmosphere can be written using two equivalent and similar expressions. The first, original, expression is

$$N = k_1 \frac{P_d}{T} + \left(k_2 \frac{e}{T} + k_3 \frac{e}{T^2}\right) - 4.028 \cdot 10^7 \frac{n_e}{f^2} + 1.45W, \tag{2.2}$$

where P_d is the partial pressure of dry air in hPa, T is the temperature in Kelvin and e is the partial pressure of water vapour in hPa. The constants are $k_1 = 77.6$ K hPa^{-1}, $k_2 = 71.6$ K hPa^{-1} and $k_3 = 3.75 \cdot 10^5$ K^2 hPa^{-1}. These constants are considered to be accurate to 0.5% of N. The electron density per m^3 is expressed by n_e, f is the radar frequency ($\sim$5.3 GHz) and W is the liquid water content in g/m^3.

Assuming that the total atmospheric pressure $P = P_d + e$, a second, equivalent, expression for N is

$$N = \underbrace{k_1 \frac{P}{T}}_{\text{Hydrostatic term}} + \underbrace{\left(k_2' \frac{e}{T} + k_3 \frac{e}{T^2} \right)}_{\text{Wet term}} \underbrace{-4.028 \cdot 10^7 \frac{n_e}{f^2}}_{\text{Ionospheric term}} + \underbrace{1.45W}_{\text{Liquid term}}, \qquad (2.3)$$

where P is the total atmospheric pressure in hPa, and

$$k_2' = k_2 - \frac{R_d}{R_v} k_1 = 23.3 \quad [\text{K hPa}^{-1}], \qquad (2.4)$$

with $R_d = 287.053$ J K^{-1} and $R_v = 461.524$ J K^{-1}. In (2.3), the first term at the right-hand side is labelled as the hydrostatic term, and the next two terms as the wet terms. The last two terms are the ionospheric term and the liquid term, respectively.

The partial pressure of water vapour, e, relates to the relative humidity, RH, by

$$RH = \frac{e}{e_s}. \qquad (2.5)$$

The Clausius-Clapeyron equation expresses the saturation pressure for a certain temperature, e_s,

$$e_s = e_0 \exp \left(\frac{L}{R_v} \left[\frac{1}{T_0} - \frac{1}{T} \right] \right), \qquad (2.6)$$

where $e_0 = 6.11$ hPa, $T_0 = 273.16$ K, T is the temperature in Kelvin, and L is the latent heat. Over a flat water surface, $L = 2.5 \cdot 10^6$ J kg^{-1}, which is the latent heat of vapourisation. In this case, cloud droplets are being formed.

The contribution in the refractivity and in the interferograms of each of the terms is:

- Hydrostatic term: The behaviour of the hydrostatic phase delay in interferograms is smooth, because of the large scales and the smoothness of the distribution of pressure in the atmosphere. Consequently, the influence of the hydrostatic delay on interferograms is limited.

- Wet term: It depends on the partial pressure of water vapour e, and on the temperature T. Its spatial variation is much more important than that of the hydrostatic term. This is due to the fact that local concentrations of water vapour vary between 0-4%, which makes it one of the most varying atmospheric constituents.

  Besides, the sensitivity the refractivity is at least 4-20 times more sensitive to a 1 hPa change in e than to a 1°C change in T. Therefore, the variations of the wet component noticeably influence the observed interferometric phase delay.

- Liquid term: The contribution of liquid water droplets is normally neglected, since it is only a small part (estimated 1-5%) of the total wet delay. Some kind of clouds and rain will affect the water vapour quantities, although the phase delay differences due to the strong water vapour gradients will be more important.

- Ionospheric term: In spite of the fact that the electron density is temporally and spatially variable, the ionosphere is often regarded as a spherical shell between 50 and 600 km height, with a constant electron density in height and homogeneously varying in time. Radio signals passing through the ionosphere are dispersively delayed by interaction with the free electrons.

  Under the hypothesis of the effects of the ionosphere resulting in long wavelength gradients over SAR images, they will not considerably affect phase variations at scales lower than $\sim$50 km.

In conclusion, the variation in the integrated refractivity is mainly due to the spatial variation of water vapour during the two SAR image acquisitions. To a lower degree temperature, liquid water, and pressure gradients influence the delay variation.

Chapter 3

Theory of SAR interferometry

3.1 Basics of SAR

A Synthetic Aperture Radar (SAR) is a remote sensing system that enables to obtain images of land surfaces. As its name indicates, it is based on a radar system, which uses the echo received from the reflection of electromagnetic pulses in a target. The term of synthetic aperture means that the system uses a processing technique to improve the resolution of the images obtained.

SAR systems work at microwave frequencies, being able to work both day and night. Their radar pulse is coherent, that is, it provides information in amplitude (reflectivity of the scene) and phase (characteristics of the path).

A SAR can be mounted on a plane (airborne SAR) or on a low orbit satellite (space-borne SAR). This project focuses on space-borne SAR systems. They obtain the images at a greater height than a plane, between 500 and 800 km. Thus, they can monitor great extensions of land, but with the drawback of a lower resolution with respect to airborne SAR systems. They are useful for applications such as the detection of a target or the calculation of the velocity of subsidence of a land with an accuracy of millimeters.

The experimental results of this study use information extracted from the SAR systems on the satellites ERS-1, ERS-2 and ENVISAT of the European Space Agency (ESA).
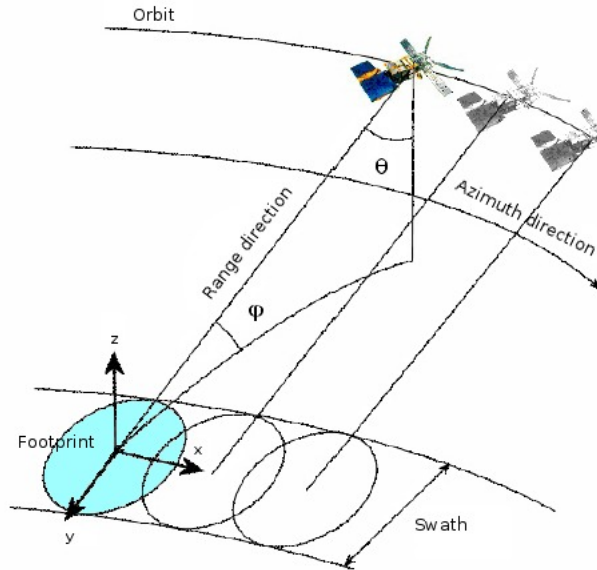
Figure 3.1: Description of the geometry strip map mode of a space-borne SAR system. The radar transmits pulses towards the earth's surface, each of which is reflected in an piece of land, the footprint, while the satellite advances on its trajectory.

3.1.1 Acquisition geometry of a SAR system

A great advantage of a space-borne SAR system over an airborne one is the ease of specification of the parameters relating to the acquisition geometry of the images. A space-borne SAR system can use different methods to acquire data; the method employed to obtain the data used in this project is called Strip Map Mode [4]. Its main characteristic is that the antenna of the radar points at a fixed position with respect to the trajectory of the satellite, as described in Figure 3.1.

The radar transmits pulses towards the surface with a frequency given by the PRF (Pulse Repetition Frequency). Each transmitted pulse is reflected in an area of the land, the footprint. The SAR sensor receives their echoes, sampled at a fixed frequency, f_s, while the satellite moves forward on its trajectory. The transmitter points at one side of the satellite to avoid right-left ambiguity in the reflected signal. Therefore, the SAR system obtains a row of the image every $1/PRF$, made up of samples obtained every $1/f_s$ seconds. Seen from another point of view, each row represents a position of the satellite in its trajectory and each sample, an instant of the received signal.

Section 3.1.2 elaborates on the possibility to combine different rows coherently
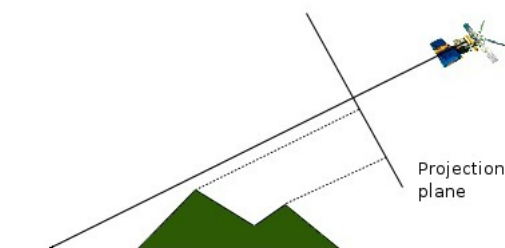
Figure 3.2: Projection plane of an optical sensor.
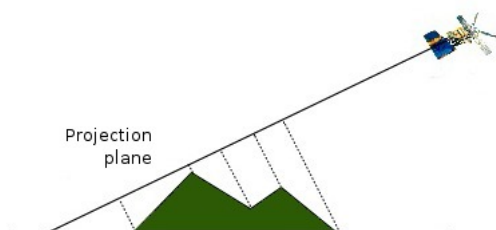
Figure 3.3: Projection plane of a radar sensor.

in order to get a row with a higher resolution, which will be part of the image known as Single Look Complex (SLC), needed for the interferometric processing.

SAR images are the projection onto the plane of acquisition of the satellite, known as the slant-range plane, of the illuminated surface, ground-range plane. This kind of projection is different to the projection that an optical sensor produces, as illustrated in Figure 3.2 and Figure 3.3.

Taking the origin of the coordinates system as the sensor of the radar, two main axis define the slant-range plane: the direction of the trajectory of the satellite, called azimuth, and the direction in which the radar pulse propagates, called range. Hence, the angle over the vertical of this plane fits in with the angle of incidence of the electromagnetic pulse with respect to the vertical, also known as the off-nadir angle θ.

The axis of coordinates referring to the ground-range plane are: the x direction, which marks the direction of advance of the area scanned by the satellite, called swath; the y direction, which is perpendicular to the x direction over the ground; and the z direction, which is perpendicular to the Earth's surface.
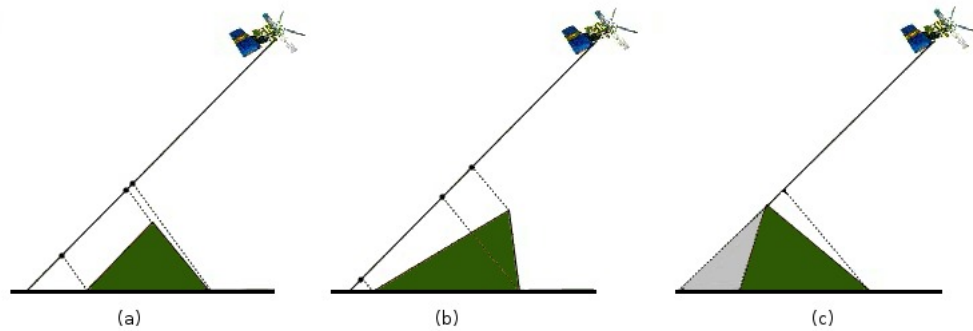
Figure 3.4: Representation of the effects intrinsics of the SAR geometry: (a) Fore-shortening, (b) Layover and (c) Shadowing.

The projection of the desired ground-range image onto the slant-range plane produces some effects over the image, preventing from having a faithful perception of the illuminated surface. These effects, intrinsics to the SAR acquisition geometry, are:

Foreshortening It is the spatial distortion whereby a slope facing the radar is mapped as having a compressed scale relative to its appearance. This effect becomes accentuated when the angle of the slope is similar to the angle of incidence, θ. In the extreme case, if both angles are equal, the slope is compressed into a point.

Layover It is the effect produced when the angle of the slope facing the radar is bigger than θ. In this case, the radar receives points in higher positions before than in lower positions, resulting in the image being out of order with respect to the reality. Ambiguity occur between targets hit at different heights, when they have the same slant-range distance. Geocoding can not resolve the ambiguities due to the representation of several points on the ground by one single point on the image.

Shadowing When a slope not facing the radar has a higher inclination than the angle of incidence over the horizontal (φ), a part of the land is not illuminated by the radar pulse (shadow zone), so there is not information of the reflectivity of this zone.

In space-borne systems, such as ERS or ENVISAT, the most common effect is the layover.

3.1.2 Basics of SAR processing

The radar of SAR systems obtain images, so-called raw data, which can be treated as a matrix of complex values, since the scanning frequency in range (f_m[1]) is much higher than the scanning frequency in azimuth (PRF[2]). The rows of this matrix correspond to the azimuth dimension, known as lines, where each line indicates a position of the satellite, whereas the columns correspond to the range dimension, where each column is a sample of the sampled pulse.

The calculation of the term of maximum resolution gives an idea of the characteristics of these raw data images. It is the minimum separation between two targets to be detected individually [5].

In the range direction, the resolution is given by

$$\Delta r = \frac{v_p \cdot \tau_p}{2}. \tag{3.1}$$

The range resolution only depends on the length of the electromagnetic pulse (τ_p), which is directly related to the bandwidth. v_p is the speed of propagation (almost that of the light in vacuum). This resolution is in the slant-range plane.

In the azimuth direction, the resolution is

$$\Delta x = \frac{R \cdot \lambda}{L}, \tag{3.2}$$

where R is the distance between the satellite and the target (range distance), λ is the wavelength and L is the physical length of the antenna in the flight direction. R and λ are intrinsic parameters of the system, so it is clear that the resolution depends on the length of the antenna.

Substituting the specific parameters of ERS and ENVISAT in (3.1) and (3.2), raw data has resolutions around 5 km in both directions. These are poor figures, so the system has to use various techniques in order to get a much better resolution [6].

For an improvement in the range direction, the length of the pulse, τ_p, could be reduced, therefore the range resolution improved, but this involves the use of higher power transmitters. It is technologically unviable in systems where the energy is limited, such as in a satellite.

Instead, SAR systems use the concept of pulse compression with a chirp pulse. It takes advantage of the fact that the receiver employs the so-called matched filter,

---

[1]For ERS, $f_m = 18.96$ MHz, and for ENVISAT, $f_m = 19.21$ MHz.
[2]For ERS, $PRF = 1679$ Hz, and for ENVISAT, $PRF = 1652$ Hz.
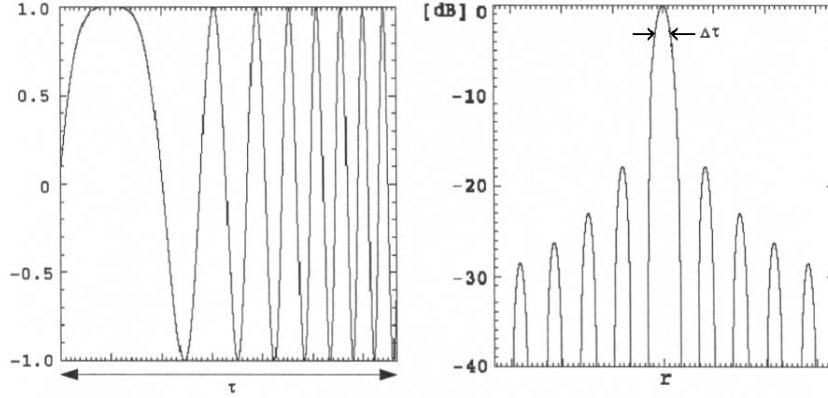
Figure 3.5: A chirp pulse and its autocorrelation. The length of chirp pulses, τ_p, is much larger than the length of its autocorrelation, $\Delta\tau_p$.

which is the optimal linear filter for maximising the signal to noise ratio (SNR). The filter is the conjugated, time-reversed version of the input signal. Thus, the output of the filter is the autocorrelation of the transmitted pulse,

$$x(t) * x^*(-t) = R_x(t). \tag{3.3}$$

The range resolution actually depends on the length of the autocorrelation, not on the length of the pulse ((3.1) uses τ_p because the length of the autocorrelation of a square pulse is the same as the length of this square pulse),

$$\Delta r' = \frac{v_p \cdot \Delta\tau_p}{2}, \tag{3.4}$$

in this way, although the length of chirp pulses, τ_p, is very large, the length of its autocorrelation, $\Delta\tau_p$, is much lower, leading to a much better range resolution. Figure 3.5 shows a chirp pulse and its autocorrelation.

In the azimuth direction, an image post-processing is the solution to better the resolution, based on the concept of antenna array. An antenna array can obtain a better azimuth resolution than a single antenna of this array. However, again, the satellite can not have a lot of antennas, but it has only one. So the idea is to take advantage of the fact that the satellite follows a trajectory, therefore different points of this trajectory that share the same target can be combined coherently, getting the same effect as if the array was real. This method is known as Synthetic Aperture Radar (SAR), and Figure 3.6 describes it.

As seen in the figure, the satellite observes the target t_{obs} seconds, from t_{start} to t_{final}, while it moves forward on its trajectory. The virtual length of the antenna that observes the target is L_{SA}, which is the length corresponding to the distance
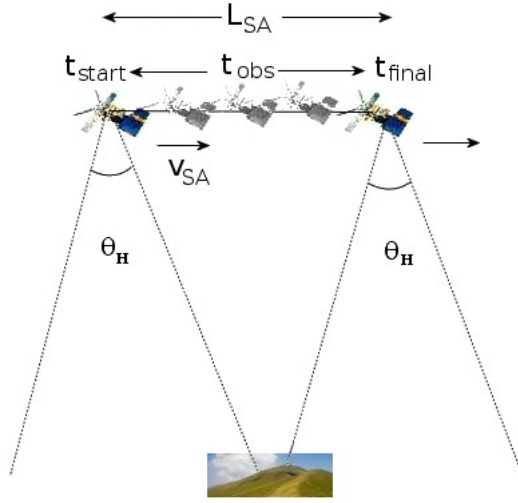
Figure 3.6: Graphical representation of a synthetic aperture. The satellite observes the target during $t_{obs} = t_{final} - t_{start}$ seconds, while it moves forward on its trajectory at a speed V_{SA}. The virtual length of the antenna that observes the target is L_{SA}, which is the length corresponding to the distance travelled during the time of observation, t_{obs}.

travelled during the time of observation, t_{obs}. Thus, the azimuth resolution of a SAR system is

$$\Delta x' = \frac{L_{azimuth}}{2}, \tag{3.5}$$

where $L_{azimuth}$ is the length of the physical antenna in the azimuth direction. Consequently, SAR processing give an azimuth resolution of the order of the antenna mounted in the satellite, independently of the range distance, the wavelength or the speed of the sensor.

Finally, the result of the processing of raw data (with low resolution) is an image with a high resolution, called SLC. SLC images are the starting point of interferometry. Figure 3.7 shows the reflectivity of a SLC image of Barcelona and its surrounding area.

3.2 SAR interferometry

SAR images have both information of amplitude (reflectivity) and phase (path travelled). SAR Interferometry (InSAR) [7] [8] [9] [10] [11] [12] tries to exploit the information of phase of two SLCs.

Figure 3.7: Region of the averaged module of an ERS SLC from the area of Barcelona. It shows the reflectivity of the scene. The city has a higher reflectivity (white), while the sea and the forests has a lower reflectivity (black). It is presented with a multilook of 5x25, that is, a spatial averaging of 5 samples and of 25 lines.

A classic application of InSAR is the obtaining of a Digital Elevation Model (DEM) of a particular zone. The interferometric phase, from two SLC images taken from points of view slightly different, is proportional to the topography.

3.2.1 The interferogram

The interferogram is defined by

$$I(x, y) = S_1(x, y) \cdot S_2^*(x, y), \tag{3.6}$$

where S_1 refers to one SLC, called master, S_2 to the other SLC, called slave, and I to the resulting interferogram. So, in terms of phase, $\psi(x, y)$ is the difference between the phase of the master image, $\phi_1(x, y)$, and of the slave image, $\phi_2(x, y)$,

$$\psi(x, y) = \phi_1(x, y) - \phi_2(x, y). \tag{3.7}$$

It is interesting to know which terms contribute to the phase of each SLC image:

$$\phi_{SLC} = \phi_{distance} + \phi_{dispersion} + \phi_{atmosphere} + \phi_{noise}. \tag{3.8}$$

Where:

- $\phi_{distance}$ is the phase due to the distance between the sensor and the target. For each pixel of the image, this phase is

$$\phi_{distance} = -\frac{2\pi}{\lambda} \cdot 2r. \tag{3.9}$$

  r is the distance between the sensor and the target (also known as range distance) and λ is the wavelength of emission of the radar.

- $\phi_{dispersion}$ is the term of the phase due to the reflection over the ground, which depends on each cell of resolution.

- ϕ_{noise} is the term that includes all the decorrelation factors that degrade the quality of the interferometric phase, such as thermal noise.

- $\phi_{atmosphere}$ is the phase owing to the propagation through the atmosphere. This project tries to understand its contribution in the phase and in the images.

Substituting (3.8) and (3.9) in (3.7) yields

$$\psi = \phi_1 - \phi_2 = \frac{4\pi}{\lambda} \cdot (r_2 - r_1) + \Delta\phi_{atmosphere} + \Delta\phi_{noise}. \tag{3.10}$$
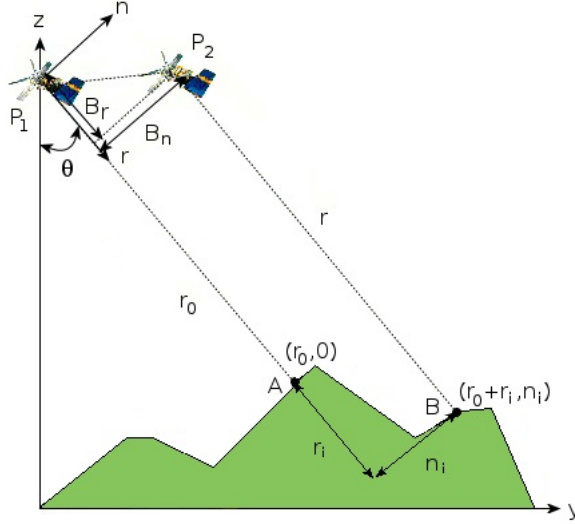
Figure 3.8: Acquisition geometry of a slant-range row for two different passes of the satellite.

Assuming that the SLCs are similar enough that they have the same phase of dispersion, the term of dispersion difference is cancelled. Thus, the interferometric phase depends essentially on the path difference between the target and both the two sensors (master and slave), respectively. Now, it is necessary to found a relationship between this distance difference and the topography of the land.

Figure 3.8 shows the acquisition geometry of a row in the range direction. The origin of coordinates is the position of the master satellite, P_1. The first direction of the coordinates following the slant-range corresponds to $\overrightarrow{r}$. On the other hand, $\overrightarrow{n}$ refers to the orthogonal direction to $\overrightarrow{r}$. Hence, from this coordinates, the position of the second satellite, P_2 is (B_r, B_n). The distance between both satellites is called spatial baseline, while B_r and B_n are the projections of the spatial baseline in the $\overrightarrow{r}$ and $\overrightarrow{n}$ directions, respectively, [13].

The points of study are A, located in $(r_0, 0)$, and B, located in $(r_0 + r_i, n_i)$, where r_0 is the distance between A and P_1, and r_i and n_i the distance between A and B in the $\overrightarrow{r}$ and $\overrightarrow{n}$ directions, respectively.

Finally, the interferometric phase difference between the point A and the point B is

$$\Delta\psi_{AB} = \frac{4\pi}{\lambda} \cdot \Delta(\Delta r) = \frac{4\pi \cdot B_n \cdot n_i}{\lambda \cdot r_0}. \tag{3.11}$$

This expression shows the interferometric phase between two points being pro-
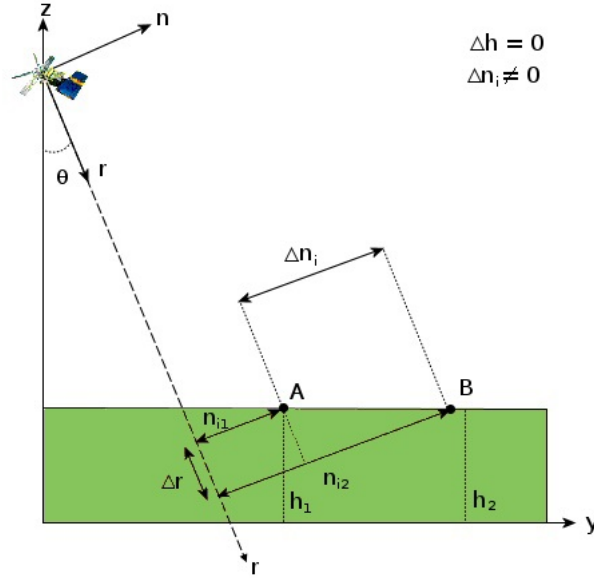
Figure 3.9: Interferometric phase obtained independently of topography, simply because the incidence angle is not 0.

portional to n_i, the distance between them in the orthogonal dimension of the slant-range plane. It is interesting to have this phase related with a more practical distance, such as the separation between the two points in the dimension that is perpendicular to the ground. To do so, the flat earth correction is carried out.

The flat earth term is the term of the interferometric phase obtained independently of topography, simply because the incidence angle is not 0. Figure 3.9 presents an example of this. In this figure, although A and B are at the same height, the interferometric phase at these points is different because the terms of perpendicular distance in the incidence plane are different.

Figure 3.10 illustrates that it is possible to divide the interferometric phase into the topographic term and the flat earth term, since n_i can be splitted into this two components,

$$n_i = n_{i,flat\,earth} + n_{i,topo} = \frac{\Delta r_{AB}}{\tan \alpha} + \frac{\Delta h_{AB}}{\sin \alpha},\qquad(3.12)$$

where Δr_{AB} is the distance between the points A and B in the slant-range plane, Δh_{AB} is the distance of height of the points A and B, and α is the incidence angle over the ground. Therefore the expression of the interferometric phase difference
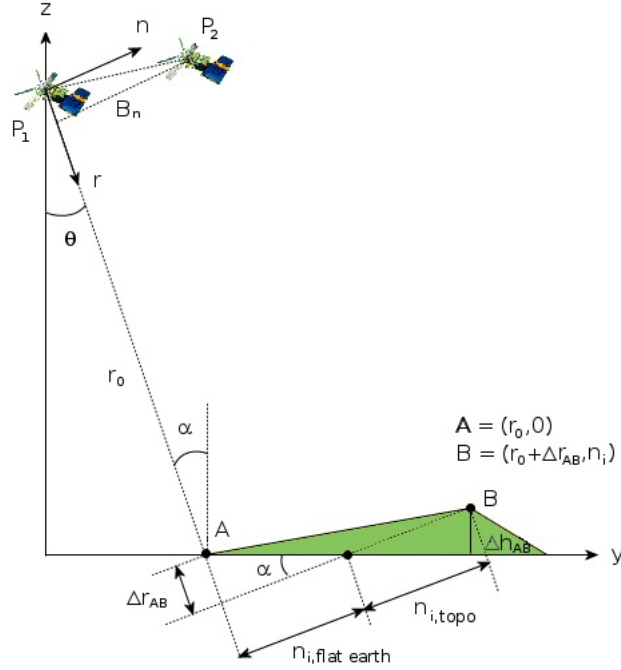
Figure 3.10: Division of the interferometric phase into the flat earth component and the topography component.

with these two contributions is

$$\Delta\psi_{AB} = \Delta\psi_{flat\,earth} + \Delta\psi_{topo} = \frac{4\pi}{\lambda \cdot r_0} \cdot B_n \cdot \left(\frac{\Delta r_{AB}}{\tan\alpha} + \frac{\Delta h_{AB}}{\sin\alpha} \right). \qquad (3.13)$$

Knowing the orbital geometry, the term of flat earth can be easily cancelled from the total interferometric phase. Subtracting it from (3.13), the difference of interferometric phase between two points depending on the topography is

$$\Delta\psi_{topo,AB} = \frac{4\pi}{\lambda \cdot r_0} \cdot B_n \cdot \frac{\Delta h_{AB}}{\sin\alpha}. \qquad (3.14)$$

Figure 3.11 presents the module of a SLC image of the area of Manresa, and the interferometric phase with and without the term of flat earth. The flat earth correction demonstrates that the term of flat earth causes the fringes of phase observed in this image. What remains describes the shape of the topography.
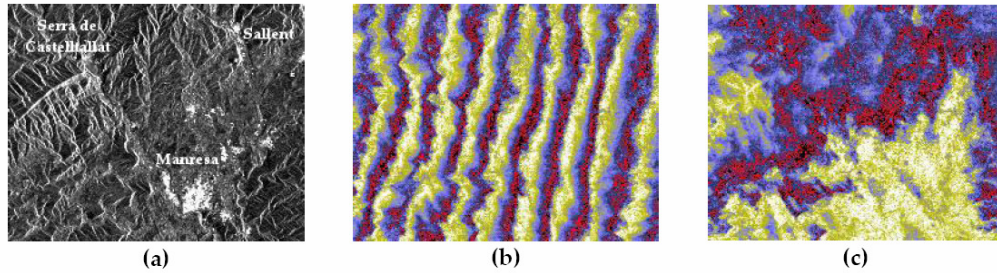
Figure 3.11: (a) Module of a SLC image of Manresa. (b) Interferometric phase corresponding to the same image, with flat earth. (c) Interferometric phase of the same image. without flat earth. The image with flat earth shows that the term of flat earth causes the regular fringes of phase observed in this image. After the extraction, what remains describes the shape of the topography.

3.3   Coherence

The quality of the results obtained from the inteferograms is basically related to the quality of the phase. The coherence is a measure of the quality of this phase. The next section elaborates on a mathematical definition of the coherence and a description of the factors that contribute to its degradation.

3.3.1   The concept of coherence

The coherence of an interferogram depends on the pixels (complex values) of each of the SLC that make up the interferogram. Taking y_1 as a pixel of the first SLC and y_2 as the respective pixel of the second SLC, the coherence between these two pixels is:

$$\gamma = \frac{E\{y_1 \cdot y_2^*\}}{\sqrt{E\{|y_1|^2\} \cdot E\{|y_2|^2\}}}, \quad 0 \leq |\gamma| \leq 1, \tag{3.15}$$

where an absolute value of coherence near to 1 indicates a good quality of phase, but if it is close to 0 it means that the scene is very noisy.

Despite this equation, in practice a spatial average substitutes the expectation operator, because the calculation of the expectation is only possible with a set of independent realisations, which is unviable. This way, an average of the pixels with a window of M samples by L rows performs the value of the estimation of γ. Moreover, multilook averaging helps to decrease speckle [14] [15], a multiplicative and random effect present in SAR images, due to the coherent addition of the

35

echoes of every targets within the same resolution cell.

$$\hat{\gamma} = \frac{\sum\limits_{i=0}^{M-1} \sum\limits_{j=0}^{L-1} y_1(i,j) \cdot y_2^*(i,j)}{\sqrt{\left(\sum\limits_{i=0}^{M-1} \sum\limits_{j=0}^{L-1} |y_1(i,j)|^2\right) \cdot \left(\sum\limits_{i=0}^{M-1} \sum\limits_{j=0}^{L-1} |y_2(i,j)|^2\right)}}, \quad 0 \leq |\hat{\gamma}| \leq 1. \qquad (3.16)$$

Figure 3.12 displays a map of coherence, of the area of Barcelona, corresponding to the region showed in the SLC image of Figure 3.7. The temporal separation is around 2 years, and because of this there is a remarkable difference between the more coherent zones and the less coherent ones. A good phase quality is indicated by white colours, whereas a lower quality by black colours. White zones refer, generally, to urban areas, because in these areas there are less changes, while black zones refer to changeable areas, such as the sea, in the right part of the figure. In order to obtain this map of coherence, the spatial averaging uses a window of $M = 5$ and $L = 25$.

3.3.2 Factors that affect the coherence

There are various factors that have an influence on the phase of an interferogram, therefore modifying its quality, or coherence:

- Noise inherent to the SAR system: It is the common thermal and system noise found in any system.

- Spatial and temporal decorrelation: In previous sections, (3.10) assumed that the term of phase of the SLC due to the reflectivity of the piece of land, $\phi_{dispersion}$, is the same for both SLCs, so when calculating the interferometric phase their difference is cancelled. In the reality, it is not in this way, because:

    - Temporal decorrelation: There is a temporal separation between the acquisition of the SLC images of an interferogram. In this time, the reflectivity of the land can have changed, so can the phase components of each SLC. This effect is the temporal decorrelation, and the only way to decrease its effects is having the temporal baseline (difference of time between the SLCs) as small as possible.
    - Geometric decorrelation: Interferometry lies in the idea of observing the scene from two different points of view. This leads to two different incidence angle, so the projection of both images onto the slant-range plane is different as well. More specifically, one image is compressed with respect to the other, as observed in Figure 3.13a. In the spectral
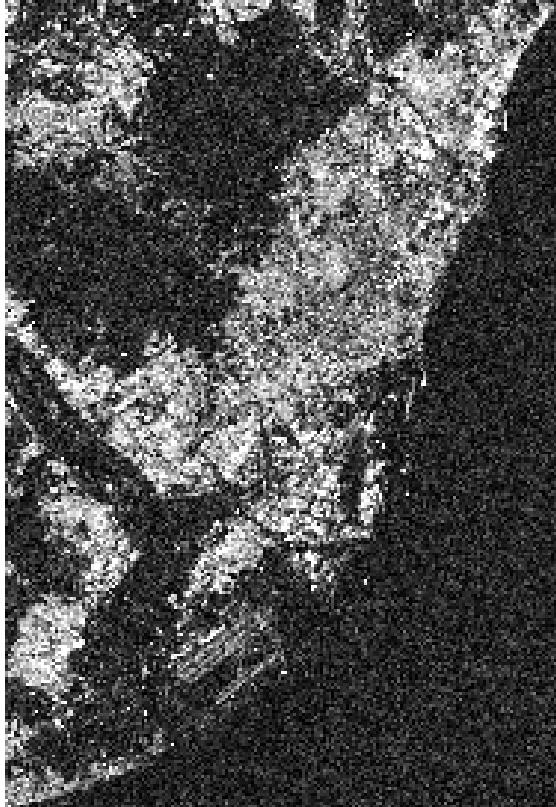
Figure 3.12: Coherence of an interferogram of the area of Barcelona, with a the temporal separation of around 2 years. White zones (good phase quality) refer, generally, to urban areas, because in these areas there are less changes, while black zones (lower phase quality) refer to changeable areas, such as the sea, in the right part of the figure. The values of M and L used to obtain this coherence are 5 and 25, respectively.
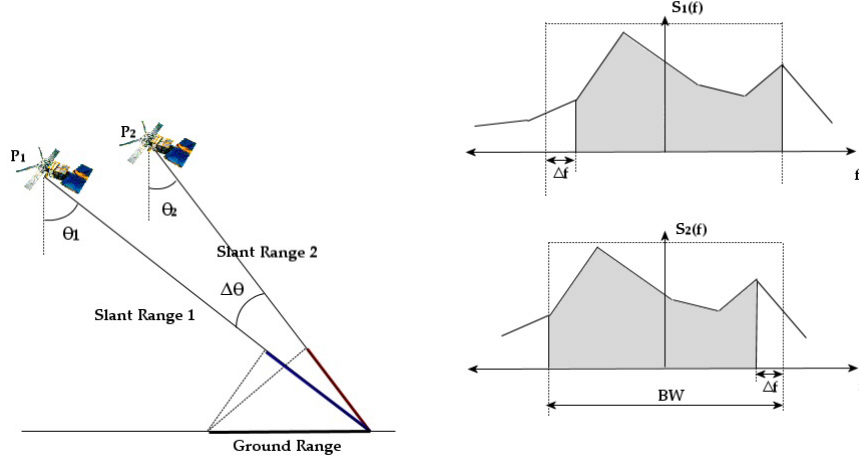
(a) Temporal compression due to the variation in the incidence angle.

(b) Spectral shift in the frequency domain because of the temporal compression.

domain, this effect means an expansion of the spectrum, but considering SAR systems as narrow-band systems, they can interpret the effect as a shift of the spectrum, as illustrated in Figure 3.13b. This effect is known as spatial decorrelation.

The expression of the shift in frequency [16] is defined by

$$\Delta f = \frac{f_0 \cdot B_n}{r_o \cdot \tan(\theta - \alpha)},\qquad(3.17)$$

where f_0 is the carrier frequency, f_0 is the distance between the satellites and the ground, B_n is the perpendicular spatial baseline, θ is the incidence angle and α the local slope.

When generating the interferogram, only the spectrum that is common in both images is useful, the rest is considered noise. If the spatial baseline is very big, there will not be overlapping between the spectra, and this threshold is the critical baseline.

- Pixel misregistration: It is possible that the pixels corresponding to two images do not represent exactly the same area of land and, therefore, the phases subtracted come from different targets. This effect can be corrected by means of a coregistration of the images.

- Doppler frequency: the shift of the spectrum in the azimuth direction due to different Doppler frequencies inherent to each SLC will cause an analogous effect to the one caused by the difference of incidence angles in the range direction. When needed, a solution is to perform a band-pass filter in the azimuth direction.
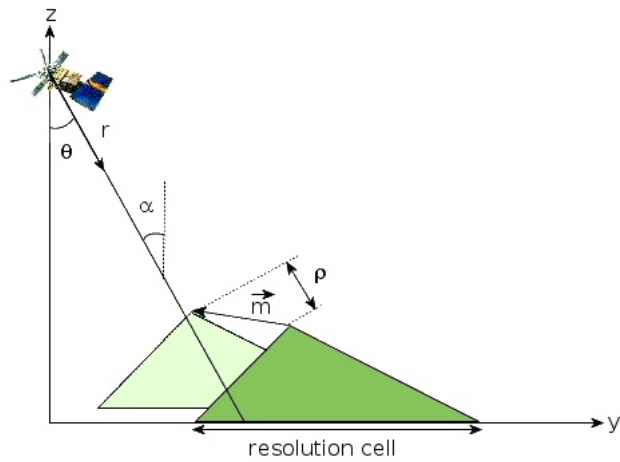
Figure 3.13: Geometry of SAR differential interferometry, in a scenario where a deformation occurs between the acquisitions of two SLCs, taken from the same point of view.

3.4   SAR differential interferometry

The techniques of SAR interferometry (InSAR) explained in the previous section intended to extract information about the topography of the land, i.e. a DEM. For this purpose, the ideal scenario is when the interferograms have a null temporal baseline. Therefore the interferometric phase owing to the movements in the land is cancelled, and the precision of the topography is maximum.

This section wants to elaborate on the opposite: calculating these movements of the land between the dates of acquisition of the images that make up the interferogram, leaving the topography aside. This technique is called SAR Differential Interferometry (DInSAR). Hence, the ideal case is to have images with a null spatial baseline so there is not topographic phase.

3.4.1   Classical differential interferometry

The main objective of differential interferometry is to obtain information from small movements of the land from a set of SAR acquisitions. In the case of Figure 3.13, it supposes that between the acquisitions of two SLCs, taken from the same point of view, a deformation, $\overrightarrow{m}$, occurs. Therefore, the resulting interferometric phase is proportional to the distance travelled by the point of interest in the range direction, ρ.

The interferometric phase component owing to the deformation is

$$\psi_{deformation} = \frac{4\pi}{\lambda} \cdot \rho, \qquad (3.18)$$

in this way, the interferometric phase will have a component due to the movement of the land or deformation, and another component due to the topography, as well as the atmospheric and noise components. The expression of the difference of phase between two points (A and B) is

$$\Delta\psi_{AB} = \frac{4\pi}{\lambda} \cdot \left(\frac{B_n \cdot \Delta r_{AB}}{r_0 \cdot \tan\theta} + \frac{B_n \cdot \Delta h_{AB}}{r_0 \cdot \sin\alpha} + \Delta\rho \right) + \Delta\psi_{atmos} + \Delta\psi_{noise}. \quad (3.19)$$

Different terms of the last equation can be easily cancelled. First, as explained before, the orbital information enables to eliminate the flat earth component. To cancel the topography, the usual technique is to use an external DEM to create a synthetic interferogram, whose phase is calculated and later subtracted from the total phase. However, the DEM can have a certain error, $\varepsilon_{DEM} = \Delta h - \Delta h'$.

After this cancellations, the interferometric phase difference is

$$\Delta\psi_{dif} = \frac{4\pi}{\lambda} \cdot \frac{B_n \cdot \varepsilon_{DEM}}{r_0 \cdot \sin\alpha} + \frac{4\pi}{\lambda} \cdot \Delta\rho + \Delta\psi_{atmos} + \Delta\psi_{noise}. \qquad (3.20)$$

3.4.2 Coherence of the differential interferogram

The differential interferometric phase, given by (3.20), does not include the terms of flat earth or the topography, so the calculation of the coherence of the differential interferogram is more polished than in (3.15). This coherence is

$$\gamma = \frac{E\{y_1 \cdot y_2^* \cdot e^{-j\cdot\phi_{topo+flat\,earth}}\}}{\sqrt{E\{|y_1|^2\} \cdot E\{|y_2|^2\}}}, \qquad (3.21)$$

where y_1 is the pixel corresponding to the master SLC, y_2 is the same pixel of the slave SLC and γ the coherence without topography and flat earth. In practice, a pixel average will replace the expectation operator.

3.4.3 Advanced differential interferometry

Classical differential interferometry aims to extract the information of the deformation of the land between the dates of the acquisitions that make up the differential interferogram. As explained before, the differential phase contains the components owing to the atmosphere and noise. In order to get better results, advanced

differential interferometry tries to isolate or at least minimise these components, because they are masking useful information.

The goal of the advanced differential interferometry is to take advantage of the redundancy of a set of differential interferograms so as to obtain a temporal evolution of the deformation. Indirectly, advanced DInSAR has to estimate the atmospheric component of the interferometric phase, by means of techniques of spatial and temporal filtering.

The algorithm of differential interferometry used to obtain the interferograms of this study is the CPT (Coherent Pixels Technique), developed by the Remote Sensing Lab (RSLab) of the Department of Signal and Communication Theory (TSC) of the Polytechnical University of Catalonia (UPC). How it works is explained next.

Pixel selection and triangulation

Only a portion of the pixels of the differential interferograms have enough quality to give useful information. For this reason, the first step is to select a set of pixels with a minimum level of quality. There are many options to do the selection, but this project uses the coherence selection, where the selected pixels have a coherence higher than a certain threshold in a % of the interferograms. A drawback of this method is that there is a loss in the resolution, but, on the other hand, its results are satisfactory with few interferograms, such as the case of this project.

After the pixel selection, there is a map of selected points as well as a set of differential interferograms with the information of phase at those points. However, each interferogram has a different phase offset, therefore it is not possible to work with absolute phases but with relative phases. To solve it, the method creates links between the different pixels and associates an increase of phase for each link. Delaunay's Triangulation [17] is the base to create this set of links, which is made up of triangular, not-overlapped relationships between the selected points.

Calculation of the linear velocity of deformation

The velocity of deformation is divided in two terms: a linear velocity and a non-linear velocity.

The first components that needs to be extracted from the interferometric phase are the linear velocity of deformation and the DEM error [18]. A model of phase including these components is created, $\Delta\psi_{model}$. It contains the values of linear velocity and DEM error that better fits to the actual interferometric phase, for

each pixel of the selection.

Concept of residual phase. Atmospheric artifacts

Separating the information to be cancelled, the expression of the interferometric phase difference is

$$\Delta\psi_{dif} = \frac{4\pi}{\lambda} \cdot T_i \cdot v + \frac{4\pi}{\lambda \cdot r \cdot \sin\alpha} \cdot B_i \cdot \varepsilon_h + \Delta\psi_{atm} + \Delta\psi_{nlm} + \Delta\psi_{noise}, \quad (3.22)$$

where T_i is the temporal baseline of the interferogram i, B_i is the perpendicular spatial baseline of the interferogram i, ε_h is the DEM error, v is the velocity of deformation, $\Delta\psi_{atm}$ is the phase component due to the atmospheric artifacts, $\Delta\psi_{nlm}$ is the phase component owing to the non-linear movement of deformation in the range direction and $\Delta\psi_{noise}$ is the phase component because of the noise and other factors (orbital errors, decorrelation...).

The previous section explains that a model synthesises the component of the linear velocity and of the DEM error, so it can be subtracted from (3.22), obtaining the so-called residue or residual phase,

$$\Delta\psi_{residue} = \Delta\psi_{dif} - \Delta\psi_{model} = \Delta\psi_{atm} + \Delta\psi_{nlm} + \Delta\psi_{noise}. \quad (3.23)$$

After this, there is one residue corresponding to each interferogram. So far, it is interesting to isolate the atmospheric phase from the phase of the non-linear movement of deformation. This task is possible because each component has its own spectral characteristics. Figure 3.14 illustrates this.

First, the atmospheric phase is due to the presence of the earth's atmosphere between the satellite and the area of observation. The main factor that generates this phase is the water vapour accumulated in the troposphere, as explained in 2.6. The behaviour of the atmosphere does not change between nearby points, so it is low-pass in space. However, its temporal behaviour is like that of white noise [19].

Second, the phase caused by the non-linear movement of deformation is the component of the deformation in the range direction that is not linear. The non-linear movement of deformation is low-pass in time.

The extraction of the atmospheric component requires low-pass filtering in the spatial domain. Therefore, the residue low-pass filtered consists of the atmospheric component of the phase and the low frequential term of the non-linear movement,

$$(\psi_{residue})_{LP} = \psi_{atm} + (\psi_{nlm})_{LP}. \quad (3.24)$$
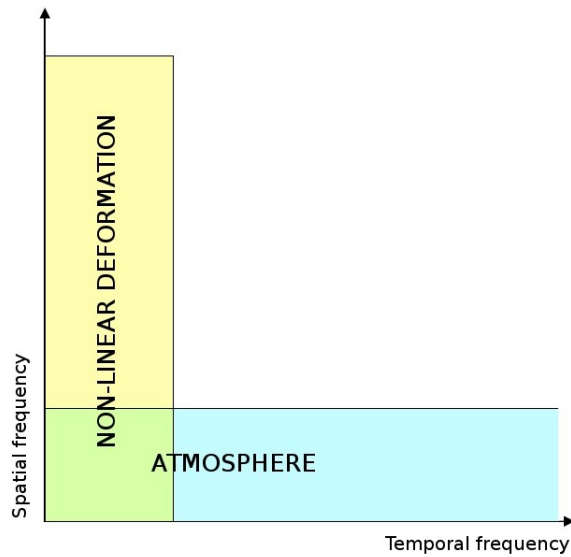
Figure 3.14: Spectral behaviour of the atmospheric artifacts and the non-linear movement. Each component has a differentiated spectral behaviour, both in time and in space: spatially, the atmosphere is low-pass while the non-linear movement is present in all the spectrum. On the contrary, in time, the non-linear movement is low-pass whereas the atmosphere is in all the spectrum.

taking into consideration that the dimensions of the spatial filter do not exceed the atmospheric correlation distance.

To obtain the atmospheric component that is not overlapped with the non-linear component, it is needed a temporal high-pass filtering to the already filtered residues, $(\psi_{residue})_{LP}$, see Figure 3.15. However, the residues refer to interferograms and these represent the information between two instants of time, so the method needs to do a temporal classification of the SLC images. The SVD algorithm (Single Value Decomposition) achieves it [20], by decomposing the residue for each one of the SLCs, and thus the filtering is easily performed.

Finally, the result is the residue of every interferogram, filtered both low-pass spatially and high-pass temporally, which is an estimation of the atmospheric component for each interferogram.

Extraction of the non-linear component of deformation

The final step of advanced differential interferometry is the extraction of the non-linear component of deformation [21], which adds to the linear component of deformation to obtain the complete evolution of the deformation of every selected
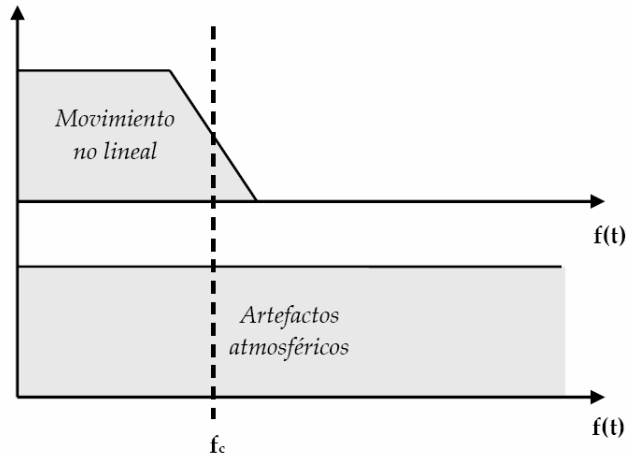
Figure 3.15: Frequential behaviour of the atmospheric artifacts and the non-linear movement.

pixels. This is the main product of advanced differential interferometry.

3.4.4 Geocodification

As seen before, all the data obtained by the radar system has the slant-range plane as its system of reference. That is, each pixel of information is related to a specific position in the orbit and to a sample in this line. Obviously, this system of presentation of the final results is not useful. A projection onto the earth's surface is better for human understanding. This is the goal of the geocodification, to present the images in a cartesian coordinate system.

The interferograms used in this project are all geocoded onto UTM coordinate system.

3.4.5 Interferometric delay analysis

The differential interferogram, (3.20), without the geographic component (flat earth and topography), depends on the deformation and on the atmospheric component of phase. Supposing that there is not deformation of land, the difference of phase can have two interpretations:

- the difference of spatial delay variation between the radar antenna and the

pixels in the interferogram, or

- the difference between the two usually uncorrelated states of the atmosphere during the two SAR acquisitions.

The relationship between the delay (in mm) and the phase is directly

$$\delta_{AB} = \frac{\lambda}{4\pi}\psi_{AB}, \tag{3.25}$$

where λ is the wavelength of emission of the radar.

Thus, the relationship between the delay observed at the resolution cells A and B, and the distribution of refractivity during the SAR acquisition, t_i, is

$$\delta_{AB}(t_i) = 10^{-6}\left(\int_A^a N\,dr - \int_B^a N\,dr\right), \tag{3.26}$$

where a is the position of the radar antenna. The antenna observes the Earth's surface with an angle of incidence.

Therefore, the delay variation, δ_{AB} observed in the interferogram can be defined as

$$\delta_{AB} = \delta_{AB}(t_1) - \delta_{AB}(t_2). \tag{3.27}$$

Therefore, the difference between two points of integrated refractivity is directly related with the delay variation, and thus, with the difference of interferometric phase between two points.

In order to compare vertical profiles of refractivity with the zenith delay, a mapping function (a cosine) should be applied to the slant delay.

Chapter 4

Developed processes

4.1 Introduction

This chapter elaborates on the process followed to generate valuable data, from which to extract useful information, by means of the processing of input data. The algorithms implemented by this project are divided in 3 points:

- Interferometric processing: It handles a set of SAR images, SLCs, in order to obtain interferograms, and later the interferometric residual phase that contains the atmospheric component. This is an intermediate result needed by the following algorithms to obtain final results.

  The software used for the generation of interferograms is called PRISAR [22], while SUBSOFT is the program responsible for producing the residue. Both processing chains have been developed at RSLab, UPC.

- Atmospheric ground data processing: Helsinki Testbed, a dense network of meteorological stations located in the area of Helsinki, supplies atmospheric measurements over the earth's surface of: temperature, relative humidity, pressure and rain; necessary to calculate the value of refractivity. This calculation will allow the estimation of a map of refractivity, since multiple stations will perform such measurements.

  Thus, the combination of two maps of refractivity, from two temporal instants, can be compared with the result of the interferometric processing, the residual phase of an interferogram from the same two temporal instants.

- Atmospheric spatial behaviour processing: This point deals with the spatial behaviour of the atmosphere, characterised by its correlation distance. The

calculation of the autocorrelation of the residues (the output of the interferometric processing chain) will enable this study.

This work studies two sets of SLCs. One of the area of Barcelona, and the other of the area of Helsinki, Finland. The set of Barcelona has 49 SLCs obtained by the satellites ERS-2 and ENVISAT, from August 1995 to December 2007, around 10:35 UTC, while the number of SLCs available for Helsinki is only 12. This images come by the satellites ENVISAT and ERS-2, from March 2004 to May 2008, around 9:15 UTC.

The code that implements the second and the third algorithms have been written exclusively for this project. The programming language employed is IDL (Interactive Data Language), a vectorised high-level language that is well-suited for the interferometric post-processing.

4.2 Interferometric processing

The objective of this section is to obtain a set of interferometric residues. Figure 4.1 displays, step by step, the method which followed in order to get the results.

Basically, the software PRISAR processes a set of SLCs, all of them corresponding to the same area of land, to generate a set of interferograms. Next, SUBSOFT handles this interferograms so as to produce the set of residual phases. The following subsections gives a detailed description of each block of the diagram.

4.2.1 Interferogram generation

First of all, as explained in Section 3.1, SLC images have information of the reflectivity of the scene (amplitude) and of the path travelled (phase). Figure 4.2 represents the averaged module of the SLC images of Helsinki (actually, a region of the SLC), or the reflectivity of the illuminated scene. An ESA software, EOLI, allows ordering SLC images of the satellites ERS and ENVISAT.

A set of SLCs corresponding to a particular area and to the same orbital track form the input of PRISAR, the software that performs the differential interferometric chain. PRISAR is in charge of the selection of suitable interferometric pairs, the the corregistration, the extraction of the flat earth and the topography of the land, and finally of the generation of the differential interferogram. It also calculates its coherence.

In practice, only a region of the SLC is processed, due to the limitation of
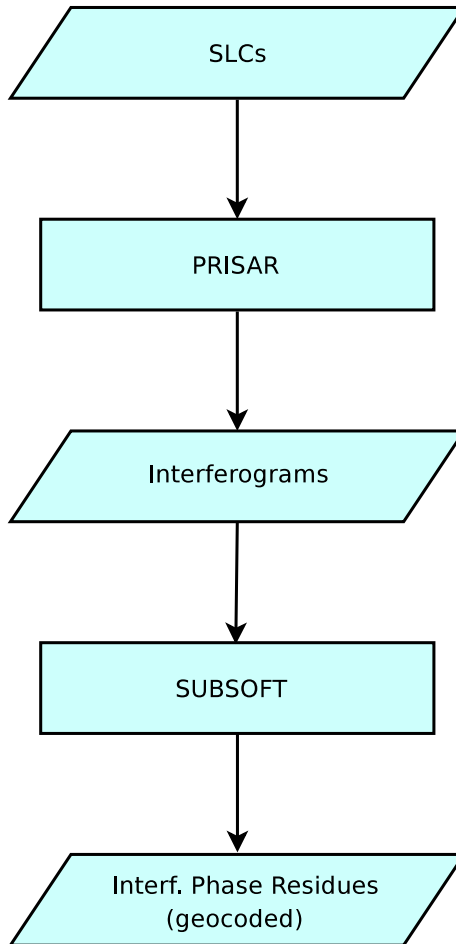
Figure 4.1: The software PRISAR processes a set of SLCs, of the same piece of land, to generate a set of interferograms. After this, SUBSOFT processes this interferograms in order to produce the set of residual phases.
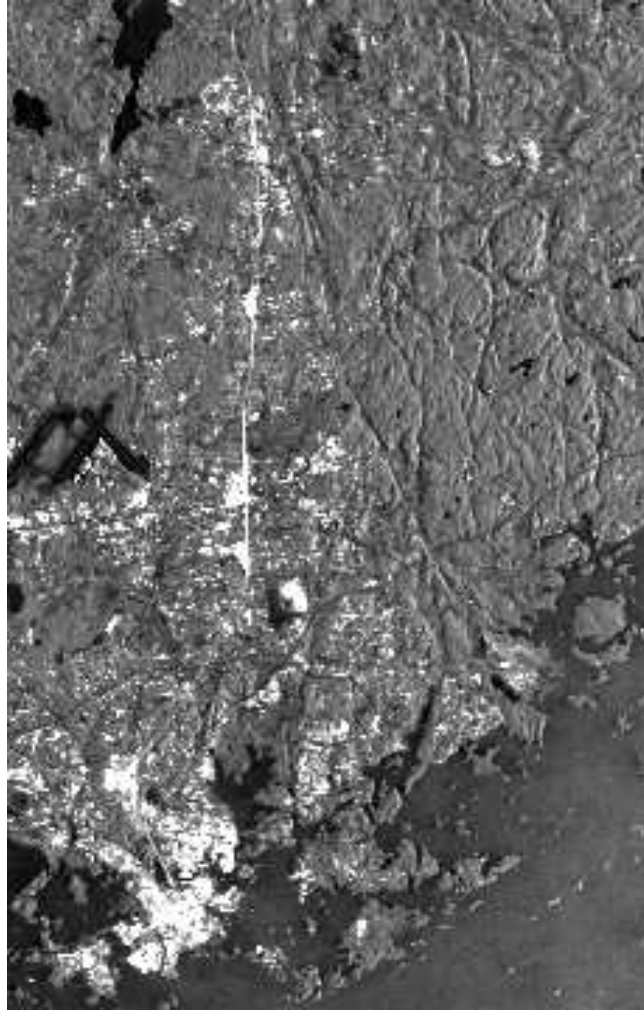
Figure 4.2: Region of the averaged module of the SLC images of the area of Helsinki, it gives information of the reflectivity of the scene. The city of Helsinki is the most reflective zone (in white), because buildings reflect the radar signal back to the antenna.

processing capacity. Usually, a region will have a maximum of 10 million of pixels. The size of the region is, 940 samples x 6820 lines in the case of Barcelona, and in Helsinki it is 1150 samples x 9000 lines.

The selection of the interferometric pairs follows these criteria (both for Helsinki and Barcelona): the maximum spatial baseline of the pair will be below 300 m, the temporal baseline below 1000 days, and the difference of doppler frequency below 1 kHz. Therefore, two SLCs will make up an interferogram if they two fulfill all the conditions.

The corregistration is the technique that makes sure that the same pixel of the SLCs that make up an interferogram correspond to the same resolution cell on the ground. Although these images should show the same piece of land, they may be slightly different, due to fluctuations of the satellite in its orbit. This causes that the images have a spatial offset between them.

Finally, after the extraction of the flat earth and of the topography, the output of PRISAR is a set of differential interferograms. Equation (3.20) gives the expression of the difference of phase between two pixels of the interferogram. Figure 4.3 shows the differential interferogram of the area of Helsinki, and Figure 4.4 its coherence.

4.2.2   Residual phase extraction

At this point, the differential interferograms are the input of SUBSOFT, which is responsible for the pixel selection, the triangulation, and for the isolation of the terms owing to the linear and non-linear velocities of deformation and to the atmosphere. This project interests are in the last component, that of the atmosphere.

SUBSOFT uses the so-called Coherent Pixels Technique (CPT) to do the pixel selection. As its names indicates, it selects the pixels by means of its value of coherence. Specifically, the pixels selected will be those whose coherence is above 0.4 in the 55 % of the interferograms of the input set in the case of Helsinki, and above 0.5 in the case of Barcelona. The map of selected points of the set of differential interferograms of Helsinki is displayed Figure 4.5, where white pixels are those that exceed the minimum quality, being a little part of the total of pixels.

The isolation of the linear velocity of deformation, a complex task, is implemented in Subsoft. It can propagate errors to the following stages in the algorithm. After this, (3.23) gives the expression of the residue, containing the atmospheric component and the non-linear component, as well as the noise component. As explained in Section 3.4.3, to get the atmospheric term, a spatial low-pass filtering
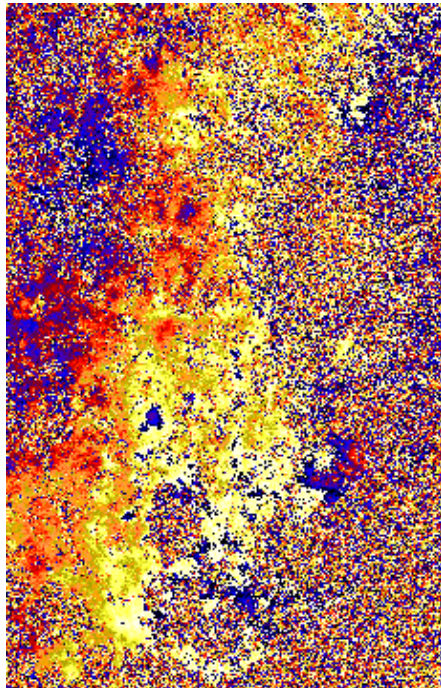
Figure 4.3: Differential interferogram of Helsinki, between the dates 20060725 and 20060829, taken by the satellite ERS-2. It has a multilook of 5x25. In the urban area (in the left), the phase is smooth, while in the sea (in the bottom right) and in forest area (in the top right) the phase is noisy.
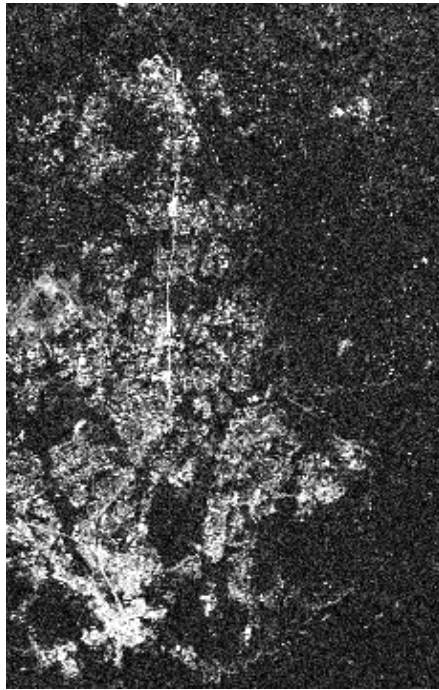
Figure 4.4: Coherence corresponding to the differential interferogram of Figure 4.3. Urban zones, with a smooth phase, have a high coherence (white). However, zones where the phase is noisy have a low coherence (black).
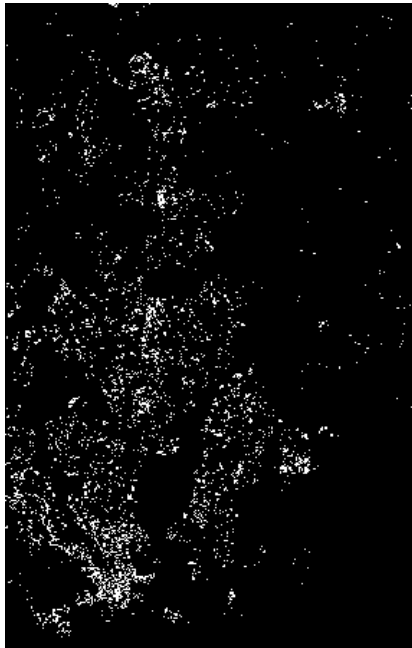
Figure 4.5: Map of selected points of the interferograms corresponding to Helsinki. A value of 1 (white) indicates that this pixel fulfill the requirements of quality, otherwise the pixel is 0. Usually, a selected point corresponds to urban areas. As seen in the previous figures, urban zones have a better quality of phase.

and a temporal high-pass filtering are needed.

To do the low-pass filtering, SUBSOFT uses a box-car window, and the selected size is 480 m, a figure lower than usual (1000 m, the assumed value of atmospheric correlation distance) in order to avoid altering the spatial behaviour of the atmosphere, which is one of the matters being studied.

The low-pass filtered residue still has a term due to the non-linear deformation in the temporal domain, see Figure 3.15. To separate them, a temporal high-pass filter is used. Residues referring to interferograms cannot be sorted, since an interferogram is a representation of the information between two instants of time. The SVD algorithm (Single Value Decomposition) solves this problem, decomposing the residue for each one of the SLCs.

The SVD algorithm needs the residual phase to be unwrapped. As the residue is spatially smooth, because of the spatial filtering applied to it, the unwrapping will be easily done with the Conjugated Gradient Method (CGM).

In this way, each one of the SLC images has an associated set of residual phases,

$$(\phi_{residue})_{LP}(t) = \begin{cases} 0 & i = 0 \\ \phi_{atm}(t_i) + (\phi_{nlm})_{LP}(t_i) - \phi_{atm}(t_0) & 1 \leq i \leq M - 1 \end{cases}, \tag{4.1}$$

where M is the number of SLCs. Although they can be put in order, it is not possible to filter them, because the SVD algorithm assigns a null value to the first image, and the filtering would eliminate this component.

To filter, the algorithm needs the value of the atmospheric component of the first image. An approximation of this component is

$$\phi_{atm}(t_0) \approx \frac{1}{M-1} \cdot \sum_{i=1}^{M-1} (\phi_{residue})_{LP}(t_i). \tag{4.2}$$

Substituting (4.2) in (4.1) enables the temporal filtering of the low-pass filtered residue.

Finally, the result is the residue of every image filtered both low-pass spatially and high-pass temporally, which is an estimation of the atmospheric component for each SLC. Figure 4.6 illustrates this atmospheric residual phase of a SLC of Helsinki, and Figure 4.7 of a SLC of Barcelona. Therefore, the atmospheric components of phase of each interferogram are simply the difference between the two components of phase of the SLC that make up the interferogram,

$$(\psi_{residue})_{LP}(t_i, t_j) = (\phi_{residue})_{LP}(t_i) - (\phi_{residue})_{LP}(t_j). \tag{4.3}$$

Figure 4.6: Interferometric residue due to the atmosphere (geocoded), in the area of Helsinki. It corresponds to the SLC taken at the instant 20070605 by the satellite ERS-2.
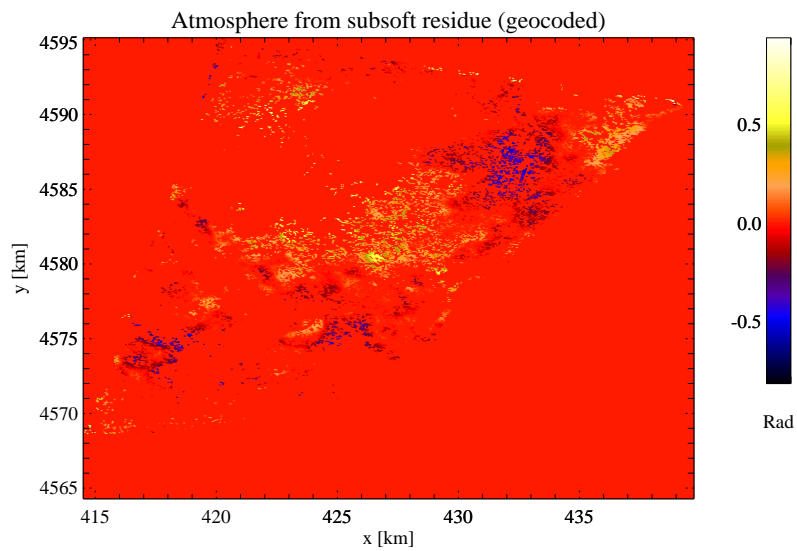
Figure 4.7: Atmospheric component of the residual phase due to the atmosphere (geocoded), in Barcelona. It corresponds to the SLC acquired at the instant 20030509 by the satellite ENVI.
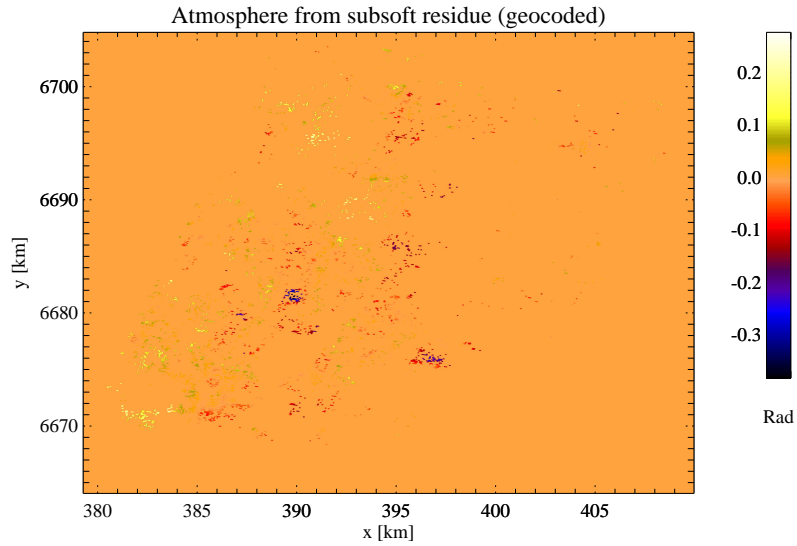
Table 4.1: PRISAR and SUBSOFT parameters used in the generation of the atmospheric residues, for Barcelona and for Helsinki. The region size determines the region within the SLC; the spatial baseline, temporal baseline and difference of doppler are used to select the interferometric pairs; the coherence is the value taken for the triangulation; and the size of the low pass-filter used to separate the atmosphere and the non-linear movement.

Parameter	Barcelona	Helsinki
Region size [samples x lines]	940 x 6820	1150 x 9000
Max spatial baseline [m]	300	300
Max temporal baseline [days]	1000	1000
Max difference of doppler [Hz]	1000	1000
Min coherence	0.5 (55 %)	0.4 (55 %)
Size of low-pass filter [m]	480	480

The process of geocodification enables to obtain the atmospheric component of the phase in the ground-range plane, in a UTM projection, instead of in the slant-range plane. The pixel size is 10x10 m. These results, the geocoded residues of the SLCs and of the interferograms, will be the input for the other processing algorithms.

4.3 Atmospheric ground data processing

The main goal of this section is to determine whether measurements of atmospheric magnitudes in the Earth's surface, such as temperature, relative humidity, pressure and rain, can serve to infer the influence of the atmospheric artifacts in the interferograms, and also to study their relationship.

Figure 4.8 shows the process to answer the previous questions. First, the Helsinki Testbed is a network of atmospheric stations, responsible for doing measurements, in the Earth's surface, of temperature, relative humidity, pressure and rain, in the area of Helsinki. The parser collects the provided data, and at the same time filters out the atmospheric measurements that are irrelevant for the purpose of this study. The useful data is sorted so as to make the next step easier, which deals with the calculation of the value of refractivity, N for each station, at a specific instant and in the surface.

These values of refractivity form a discrete map of refractivity, at a given instant. To do the comparison between refractivity and the atmospheric residue, the difference between two refractivity maps has to be done, the so-called synthetic Atmospheric Phase Screen (APS), because two SLCs obtained at different instants
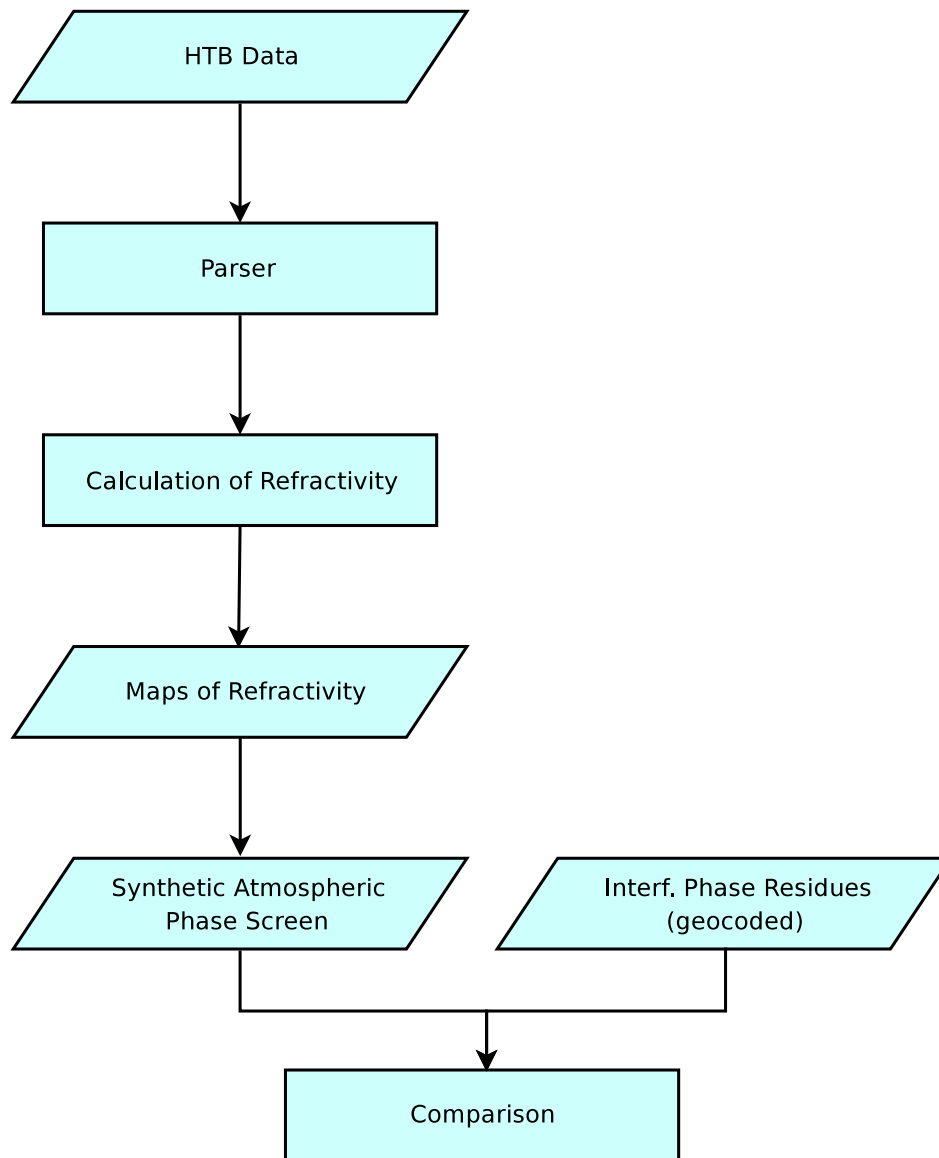
Figure 4.8: Data from the HTB is parsed and sorted, so as to calculate the value of refractivity for each station and instant. The synthetic Atmospheric Phase Screen (APS) is the difference of two maps of refractivity. Finally, the APS is compared with the atmospheric component of the residues coming from the SUBSOFT.
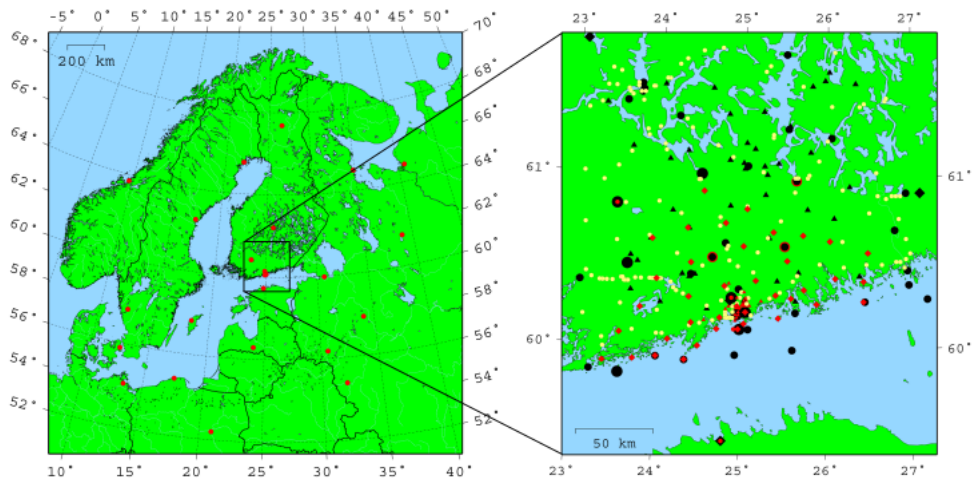
Figure 4.9: Map of the zone of Helsinki and the zoom with the location of the measurement stations. The red points are the stations that takes the measurements of interest.

make up an interferogram.

In the next subsections, there are further explanations about the steps of the diagram.

4.3.1 Helsinki Testbed data

Helsinki Testbed (HTB) is a project launched by the Finnish Meteorological Institute and the company Vaisala, whose main is the atmospheric weather research. It has different stations working in the area of Helsinki, see Figure 4.9, and measures, every 10 minutes, various atmospheric magnitudes. These measurements take place in the surface.

It provides these measurements between April 2005 and May 2007. However, there are periods, within these dates, when the stations did not work.

The format of the file containing the measurements is displayed in Figure 4.10. Each row has the measurement of a magnitude, in a station, at a specific time. The important fields are the acquisition time, the latitude and longitude of the station that performs the measurement and, obviously, the magnitude, its value and units.

The parser extracts only the useful information, and saves them in convenient

```
validtime|latitude|longitude|leveltype|levelvalue|levelunit|member|version|parname|parvalue|
parunit|aggregationname|aggregationvalue|aggregationunit|form

20060724131000|60.8154|25.0508|altitude|176|m|2|1|windspeed|5.4|m/s|average|600|seconds|n/a
20060724131000|60.292|24.3944|altitude|145|m|2|1|temperature|23.3|C|instant|0|n/a|n/a
20060724131000|60.292|24.3944|altitude|145|m|2|1|relativehumidity|45.8|%|instant|0|n/a|n/a
20060724131000|60.292|24.3944|altitude|145|m|2|1|pressure|995.5|hPa|instant|0|n/a|n/a
20060724131000|60.0761|23.5904|altitude|126|m|2|1|rainamount|0.02|mm|cumulated|24|hours|liquid
20060724131000|60.0761|23.5904|altitude|126|m|2|1|rainduration|100|seconds|cumulated|24|hours|liquid
20060724131000|60.0761|23.5904|altitude|126|m|2|1|rainintensity|0|mm/h|instant|0|n/a|liquid
```

Figure 4.10: The format of the HTB file of measurements. Each row contains the measurement of a magnitude, done in a station, at a specific time.

format: a matrix in which every row contains the position of the station, the date of acquisition, and both the temperature, relative humidity, pressure, and if it rains. In this way, grouping the measurements for station and for acquisition time, it will be easier to calculate the map of refractivity.

The information about the rain is simply a flag indicating if it rains. The calculation of refractivity will discard measurements done when raining.

4.3.2 Generation of the refractivity map

Once the parser has finished the extraction and sorting of the information, it will be the input for the program that calculates the refractivity map. Indicating the desired time instant, this program will calculate the value of refractivity, for each station, by means of (2.3), at the given time instant.

The expression to calculate the refractivity used in this project, does not use the ionospheric term, because it does not affect interferograms at a small scale, or the liquid term, as said before. Therefore, the refractivity depends on the hydrostatic term and on the wet term.

Thus, it makes up a discrete map of refractivity, at the ground level, as illustrated in Figure 4.11, shows its interpolated version. This map represents the refractivity of Helsinki and surroundings at the instant 2006-08-29, 09h30m00s.

In order to compare the refractivity with an interferogram, it needs to be taken into account that two SLCs make up an interferogram. The phase of the interferogram is the difference between the phase of each SLC. Therefore, the atmospheric component of the interferometric residue directly relates to the difference between two maps of refractivity, each of which calculated at the same instant than the acquisition time of each SLC.

The difference of two refractivity maps, with its mean value subtracted, is also
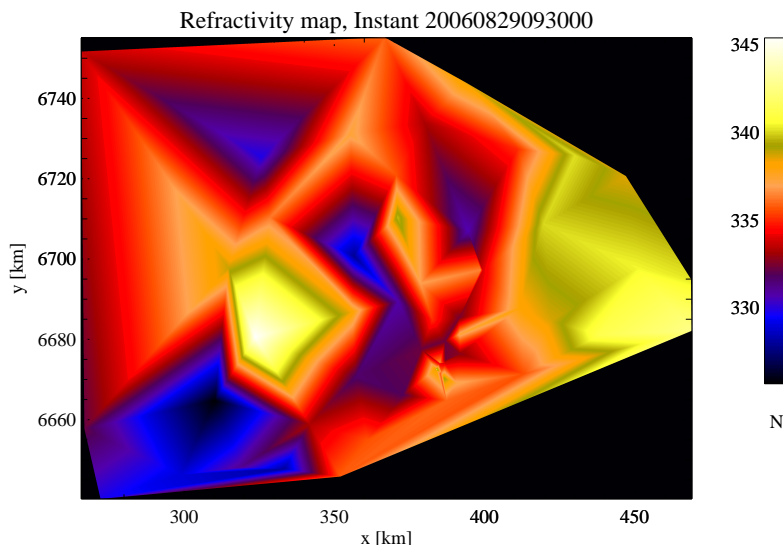
Figure 4.11: Refractivity map (interpolated) of the instant 2006-08-29, 09h30m00s, calculated from the data of the Helsinki Testbed.

known as the synthetic Atmospheric Phase Screen (or synthetic APS).

4.3.3 Comparison between the atmospheric phase and the synthetic APS

At this point, the software performs the comparison between the synthetic APS and the atmospheric component of the interferometric residue, which is the output of SUBSOFT, as explained in Section 4.2.

Equation (3.26) states that the interferometric phase difference between two points directly relates to the difference of integration of refractivity along the path, between the same two points. However, this section compares the interferometric phase due to the atmosphere with values of refractivity calculated on the surface. Although the comparison will never be perfect, it makes sense because major contributions to the refractivity take place in the troposphere, which is the lower layer of the atmosphere.

The comparison only considers the area that is common in both maps (refractivity and interferometric residue). Due to the discrete nature of both matrixes (only certain pixels of the matrix are defined), the value of difference of refractivity in the position of a specific station is compared with the an average value of the atmospheric phase at the same position. The average of the residual phase

is spatial, calculated with a box of 220x220 m centred in the coordinates of the station.

Hence, vectors are useful to represent all these values, and the position within the vectors will indicate the index of the station. So, one vector, $\overrightarrow{\psi}$, contains the values of atmospheric phase for each station, whereas the other vector, $\overrightarrow{N}$, has the values of differential refractivity for each station. In this way, the normalised euclidean distance gives a measurement of its similarity,

$$\cos \beta = \frac{\overrightarrow{\psi} \cdot \overrightarrow{N}}{||\overrightarrow{\psi}|| \cdot ||\overrightarrow{N}||}. \tag{4.4}$$

The goodness of this coefficient is validated by the comparison with the standard deviation of two gaussian random vectors, of the same length than the real data, M. This value is $\dfrac{1}{\sqrt{M}}$.

4.4 Atmospheric spatial behaviour processing

The objective of this processing is to characterise the spatial behaviour of the atmosphere, more specifically, the correlation distance of the atmosphere. This concept means that the characteristics of two points of the atmosphere are similar if their separation is below this distance, but the points are uncorrelated if the separation is above this distance. 1 km is a commonly assumed value for the correlation distance, and many interferometric software use this figure, such as SUBSOFT.

The diagram in Figure 4.12 gives a detailed view of the steps of the processing. First of all, it calculates the autocorrelation of each matrix consisting of the residual phase owing to the atmosphere, that are the output of SUBSOFT, described in Section 4.2. In this case, the project will use the residues of the SLCs, given by (4.1), instead of the residues of the interferograms. It allows doing a temporal selection.

The next step is to perform the average of the autocorrelations, with either no separation (annual) or seasonal separation. The fitting block is in charge of obtaining an analytic function that best fits the average of the autocorrelations, hence the correlation distance parameters. The final subsection discusses the validation of the method used to calculate the autocorrelation of the residue.

The following subsections elaborate on an accurate description of the diagram.

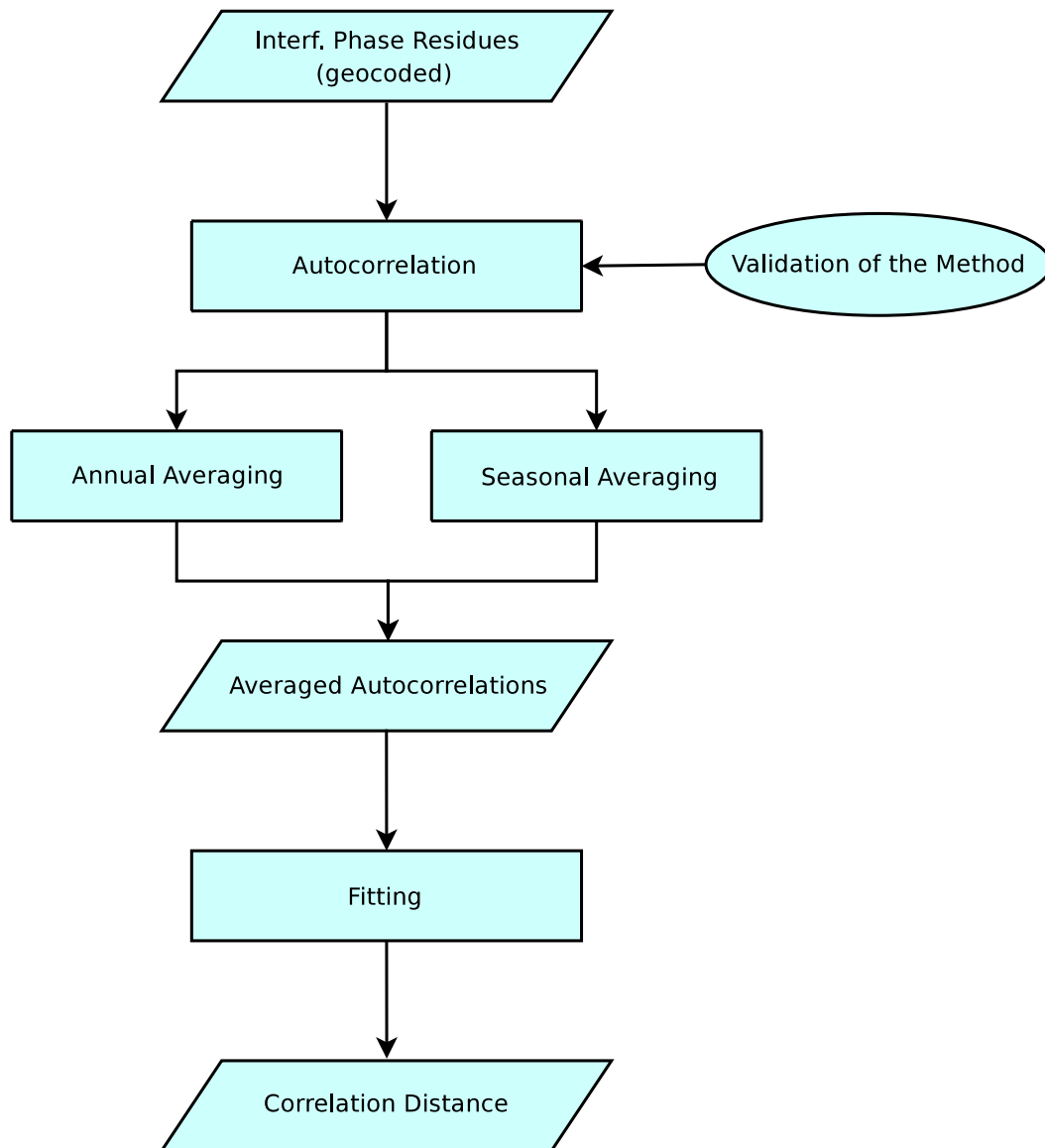Figure 4.12: The first step is to calculate the autocorrelation of each atmospheric residue (the output of SUBSOFT). Later, the next step is to do their average, allowing the temporal classification. The fitting block looks for a analytic functions that expresses the form of the average of the autocorrelations. Knowing the function parameters, it is possible to extract the correlation distance figure.

4.4.1 Calculation of the autocorrelation of the atmospheric residue

The autocorrelation of each matrix of atmospheric residue, corresponding to the SLCs, is calculated. The software performs a spatial low-pass filtering and then a decimation, because of problems of processing capacity. The resulting resolution is of 20 m (instead of 10 m).

The expression of the autocorrelation of any matrix is

$$R_X = X(n, m) * X^*(-n, -m), \qquad (4.5)$$

or analogously, working with the Fourier transform,

$$R_X = \mathcal{F}^{-1}\{|\mathcal{F}\{X(n, m)\}|^2\}, \qquad (4.6)$$

where R_X is the autocorrelation of the matrix X, and $\mathcal{F}$ and $\mathcal{F}^{-1}$ are the operators of direct and inverse Fourier transform, respectively. Nonetheless, this equation does not apply completely to our matrix of atmospheric residue, because not all the pixels have a value, only those chosen in the pixel selection.

For this reason, the project proposes another method. It relies on doing both the autocorrelation of the atmospheric residue and of the matrix of selected points. The pixel selection is equivalent to a mask, a matrix of 1s and 0s multiplying the useful data, the 1s are located where there is a value in the matrix of atmospheric residue).

After this, the complete autocorrelation is the quotient between them the autocorrelation of the masked residue and the autocorrelation of the mask,

$$R_{residue} = \frac{\mathcal{F}^{-1}\{|\mathcal{F}\{X_{masked\,residue}\}|^2\}}{\mathcal{F}^{-1}\{|\mathcal{F}\{X_{mask}\}|^2\}} = \frac{R_{masked\,residue}}{R_{mask}}, \qquad (4.7)$$

where $X_{masked\,residue}$ is the matrix of the masked atmospheric residue, and X_{mask} the matrix of the selected points. This way, we overcome the problem of our matrix not being totally defined.

Section 4.4.4 checks the validation of this method.

An example of the autocorrelation of an atmospheric phase residue of a SLC, of Barcelona, is in Figure 4.13. Specifically, the time of acquisition of the SLC is at 20000901, taken by the satellite ERS-2. Values of $R_{residue}$ obtained with a value of R_{mask} lower than a certain threshold are cancelled. Lower values of R_{mask}, due to low correlation, causes an undesired increase in values of $R_{residue}$.
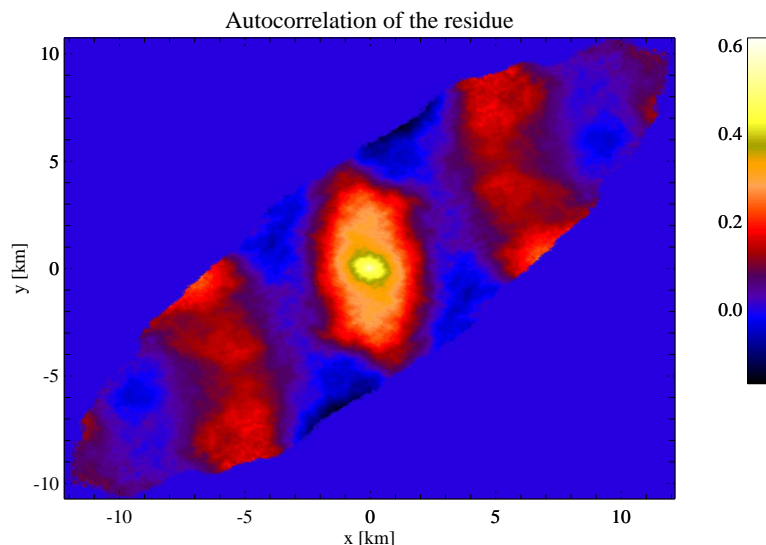
Figure 4.13: Autocorrelation of the atmospheric residue of phase of a SLC (taken at 20000901 by the satellite ERS-2) of Barcelona.

4.4.2 Autocorrelations averaging and seasonal division

The atmosphere of an single instant does not provide a statistical behaviour (except under the assumption that the process is ergodic). Therefore, the method calculates the average of all the matrixes of autocorrelation. This way, the resulting averaging contains the mean spatial behaviour of the atmosphere.

Figure 4.14 shows the average of the autocorrelation matrixes, for the case of Barcelona. The next section studies its shape. It is smoother than the single autocorrelation of Figure 4.13.

Besides the annual study, the fact that the inputs are residues of the SLCs (with known acquisition times) enables to classify them seasonally, so as to analyse if the change of climate conditions due to the seasons affects the spatial behaviour of the atmosphere.

Thus, the residues of the SLCs are divided into four groups: Winter, between 22nd December to 20th March, Spring, between 21st March to 20th June, Summer, between 21st June to 22nd September, and Autumn, between 23rd September to 21st December. For each of the four groups, the project calculates the average of the autocorrelations.

Figure 4.14: Average of the autocorrelations of the atmospheric residues, of the area of Barcelona. It has a radial symmetry.

4.4.3 Determination of the correlation distance

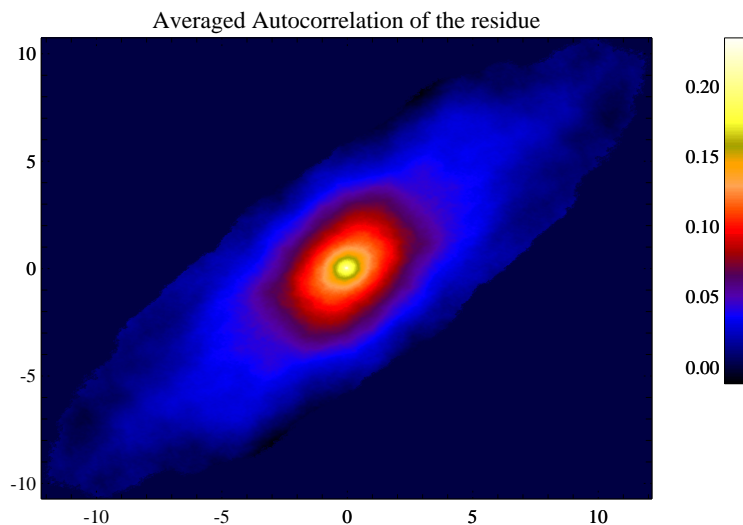At this point, there is an average of autocorrelations for each of the stations, as well as an annual average. The slices of any of this matrixes indicate that they have an exponential decay. Thus, with this form, the correlation distance is directly the position where the autocorrelation is the maximum value (that of the centre) divided by e (exp(1)).

However, as seen in Figure 4.14, the horizontal slice of the average autocorrelation is an ellipse, not a circle. Therefore, a single slice does not give the correct value of correlation distance, but the calculation needs to take into account all the slices. Figure 4.15 depicts the (different) slices, in the directions x (in red) and y (in blue), of the annual average autocorrelation of the set of residues of Barcelona.

Fitting algorithms solve this problem: they provide an analytic expression that best fits the combination of all the radial sections. As the decay is exponential, the analytic function is $a \cdot e^{b \cdot r} + c$ (assuming isotropia), and fitting algorithms give the solution for a, b and c. r is the radius vector.

To avoid the influence of the peak of the autocorrelation corresponding to noise in the positions near $r = 0$, and also to avoid the influence of the discontinuities in far-off positions, $r > 4-5$ km, the fitting will not take into consideration the values of autocorrelation whose $r < 250$ m, and whose $r > 5$ km (values of $r > 4 - 4.5$)
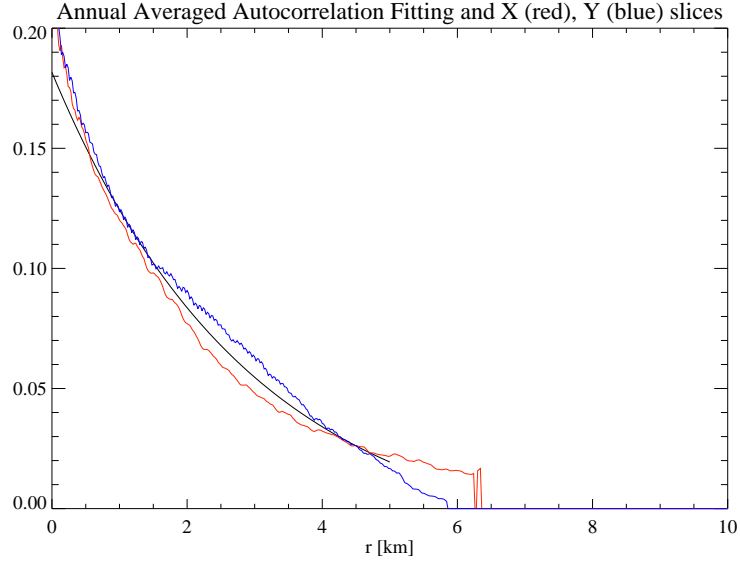
Figure 4.15: Slices, in the directions x and y, in red and in blue respectively, of the annual average autocorrelation of the set of residues of Barcelona. In black, the fitting of the autocorrelation. Visually, the three curves are very similar.

are also used, depending on the case). Figure 4.15 shows the fitting function (in black) of the annual average autocorrelation of Barcelona.

Hence, the knowledge of the function parameters, a, b and c, leads to the correlation distance, r_c, that will be

$$a \cdot e^{b \cdot r_c} + c = \frac{a+c}{e} \Rightarrow r_c = \frac{1}{b} \cdot \ln \frac{1}{a} \left(\frac{a+c}{e} - c \right) \qquad (4.8)$$

As said before, the software obtains the correlation distance for each season, as well as a generic or annual value.

4.4.4 Validation of the method to calculate the autocorrelation

This section discusses the validation of the method used to calculate the autocorrelation of the atmospheric residue, (4.7), which deals with the calculation of the autocorrelation of a masked matrix. In order to validate the method, the software of the project generates a simulated matrix with the same spectral characteristics than that of a real atmospheric residue.

The goal is to obtain a random matrix, X_{sim}, that when processed with (4.7), the result is the average of the autocorrelations of the atmospheric residues of a

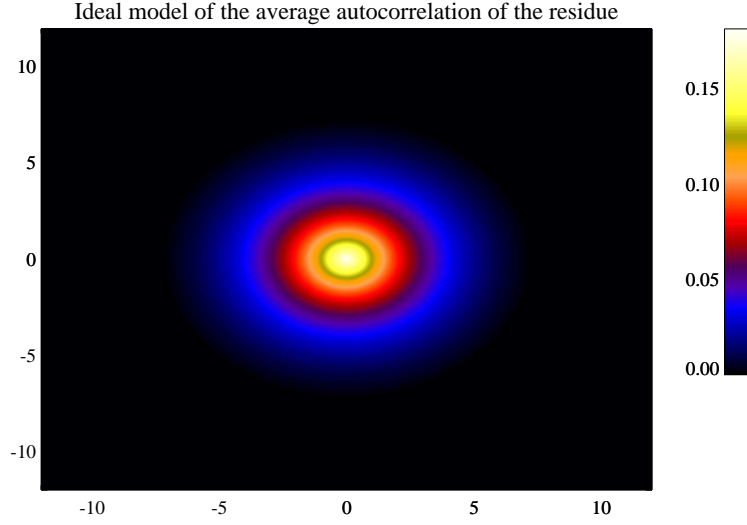Figure 4.16: Ideal average autocorrelation. The fitting function $a \cdot e^{b \cdot r} + c$, with the parameters found in the case of Barcelona, defines any radial slice of the matrix.

set of SLCs, $R_{residue,average}$. It is possible by combining a gaussian random matrix with the desired spectrum. The expression of the method is

$$X_{sim} = \mathcal{F}^{-1}\{\mathcal{F}\{X_{random}\} \cdot \underbrace{\sqrt{\mathcal{F}\{R_{residue,average}\}}}_{|\mathcal{F}\{X_{residue,average}\}|}\}, \qquad (4.9)$$

where $X_{residue,average}$ is the hypothetical matrix whose autocorrelation would be the average of the autocorrelations of the residues, $R_{residue,average}$. (4.6) relates one to the other, so the square root of the transform of $R_{residue,average}$ will be used instead of transform of $X_{residue,average}$.

The starting point is the generation of a gaussian random matrix, X_{random}, whose elements are a gaussian random variable, N(0,1), uncorrelated with each other, and whose spectrum is flat. The multiplication between the fourier transform of X_{random} and the fourier transform of $X_{residue,average}$ produces a matrix with the spectrum of $X_{residue,average}$ and the random aspect of X_{random}.

The matrix of $R_{residue,average}$ used is not the real average but its ideal form, that is, the matrix synthesised with the shape of the exponential function that fits the real average. Figure 4.16 shows the ideal average autocorrelation, whose radial section is the function $a \cdot e^{b \cdot r} + c$ with the parameters calculated for the case of Barcelona.

Finally the mask of selected points is applied to the resulting matrix, X_{sim}, re-
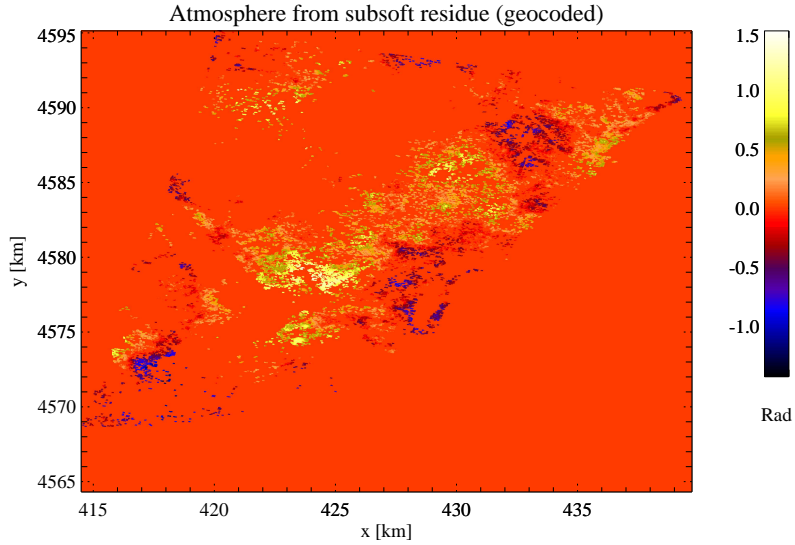
Figure 4.17: Random matrix that simulates the atmospheric component of the interferometric residue, in the area of Barcelona.

sulting in Figure 4.17 when the source is the average autocorrelation in Barcelona. This matrix is visually similar to that of Figure 4.7, a matrix displaying the atmospheric residue of a SLC of Barcelona. Both of them have the same spectral characteristics, but Figure 4.17 is totally artificial.

In order to accept the method in question, the autocorrelation of the simulated matrix, X_{sim} must be equal to the average of autocorrelations of the real atmospheric residues. The software does the so-called Monte Carlo simulations, an average of 60 autocorrelation matrixes coming from 60 different simulated atmospheric residues so as to better the estimation of the simulated autocorrelation. Figure 4.18 illustrates this, and it really looks like the ideal average autocorrelation, of Figure 4.16.

Finally, the project compares the average autocorrelation of Barcelona and of Helsinki with their respective simulated models: in the case of Barcelona, Figure 4.19 depicts the fitting curve of the real average autocorrelation (in solid black), and the fitting curve of the averaging of autocorrelations of the simulated data (in black, dotted, overlapped with the x and y slices, in red and blue); Figure 4.20 displays the same, in the case of Helsinki. The results for Helsinki are worst because the low number of SLCs available for this zone.

There is a slight difference between the fitting of the real data and the fitting of the simulated data. In terms of numbers, Table 4.2 shows the comparison (Section 5.3 will show the results of correlation distance in Barcelona and Helsinki). The

68

Autocorrelation of the residue -> random model
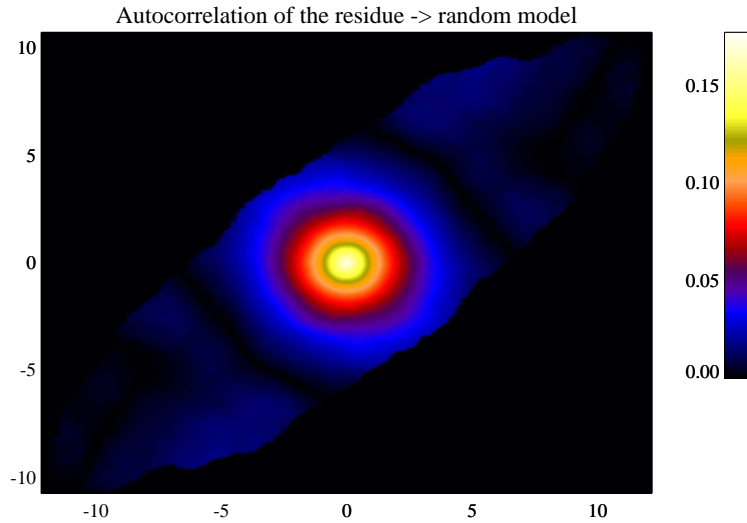
Figure 4.18: It is the average of 60 autocorrelation matrixes. One of these auto-correlation matrixes comes from a simulated atmospheric residues. It has to be equal to Figure 4.16 and, certainly, they are almost identical.

Averaged Fitting and X (red), Y (blue) individual slices
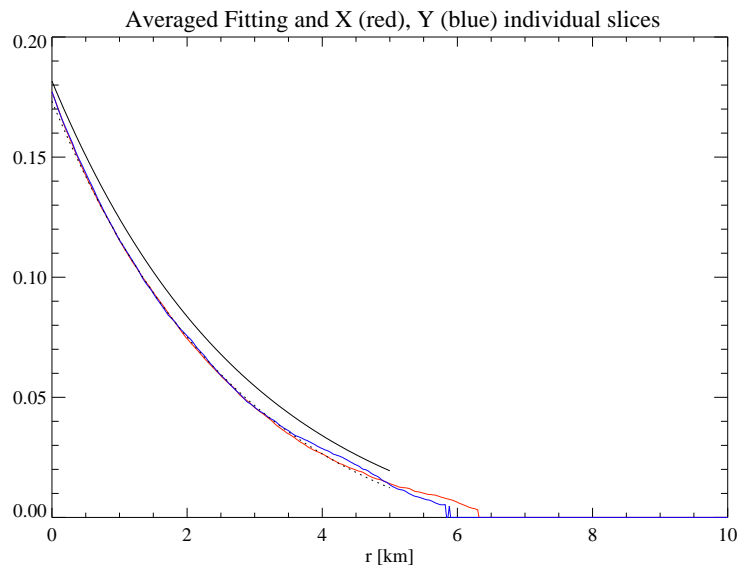
Figure 4.19: Comparison between the fitting of the averaging of the autocorrelation of the atmospheric residues of Barcelona (solid black) with the fitting of the average of the autocorrelations of the simulated atmospheric residues (dotted black) and its x and y slices (red and blue, respectively).
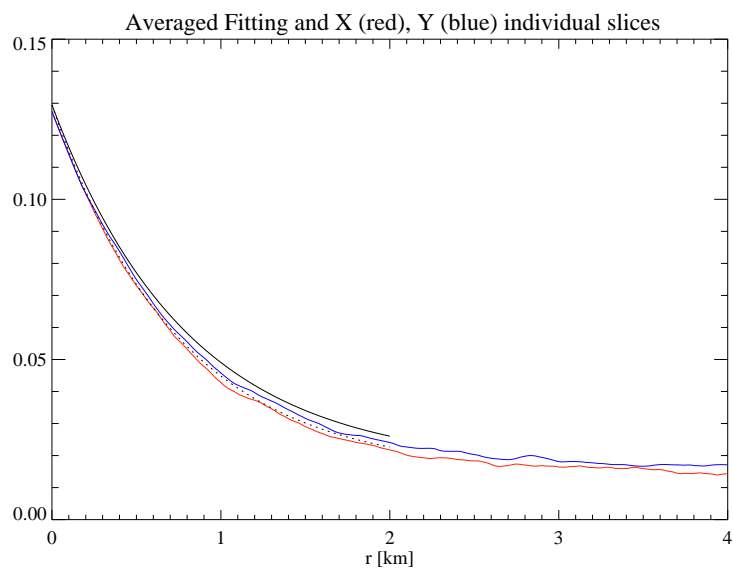
Figure 4.20: Comparison between the fitting of the average of the autocorrelation of the atmospheric residues of Helsinki (solid black) with the fitting of the average of the autocorrelations of the simulated atmospheric residues (dotted black) and its x and y slices (red and blue, respectively).

Table 4.2: Comparisons between the real and the simulated correlation distances both for the area of Barcelona and Helsinki.

Zone	Real corr. distance [km]	Simulated corr. distance [km]	Error [%]
Barcelona	2.54	2.36	7.1
Helsinki	1.04	0.94	9.6

testing is acceptable, being the error below the 10 %, and the method to calculate the autocorrelation that this project uses is, therefore, validated.

70

Chapter 5

Experimental results

5.1 Introduction

This section will present the results of the project. Chapter 4 explains the processes carried out to obtain these results. The first result comes from the algorithm called "atmospheric ground data processing", and it is the comparison between the synthetic Atmospheric Phase Screen and the atmospheric term of the residue. The second result stems from the "atmospheric spatial behaviour processing", and it is the atmospheric correlation distance, both a generic value and a seasonal value.

As an intermediate result, the "interferometric processing" provides the atmospheric residues of the interferometric residual phase, which are needed to obtain the results above mentioned. There is a set of residues of the SLC's-interferograms from Barcelona, and another set from Helsinki:

- There are 49 SLCs of Barcelona, obtained by the satellites ENVISAT and ERS-2, between August 1995 and December 2007, at 10:37 UTC. These SLCs make up 100 interferograms.

- The number of SLCs available for Helsinki is low, only 12. The images come from the satellites ENVISAT and ERS-2, between March 2004 and May 2008, acquired at 9:25 UTC. They form 11 interferograms.

5.2 Results of the atmospheric ground data processing

This section presents the results of the processing developed in Section 4.3, the comparison between the atmospheric residue and the synthetic APS. The input of measurements of atmospheric magnitudes (on the ground) leads to the generation of the synthetic Atmospheric Phase Screen, which is the difference between two refractivity maps. This APS is compared with the matrix that contains the residual phase owing to the atmosphere, which is the other input.

There are only atmospheric measurements for the area of Helsinki. Therefore, the APS must be compared with the interferometric atmospheric residue of the Helsinki set. Logically, the dates (and times) of acquisitions of the SLCs that make up the interferogram must be equal to the dates (and times) of the refractivity maps that comprise the APS.

However, the number of coincidences between the pair of dates of the interferograms and the pair of dates of the data from the HTB is low, exactly there is only one coincidence, making the study of the comparison basically theoretical. The pair of coincident dates is 2006-07-25 and 2006-08-29.

On the one hand, Figure 5.1 displays the matrix of the atmospheric residue corresponding to the interferogram composed of the SLCs taken at 2006-07-25 and 2006-08-29 (both from satellite ERS-2). Its pixel size is 40 m, and it is a cutting so that it represents the same area than the cutting of the Atmospheric Phase Screen.

On the other hand, the synthetic Atmospheric Phase Screen, in the dates 2006-07-25 and 2006-08-29, is in Figure 5.2. To make it clear, this map only represents the value at the position (and the pixels surrounding it) of the station that measures the atmospheric magnitudes. The total of stations in this matrix is 13.

5.2.1 Discussion

At first sight, one map does not resemble the other, although there is a similar tendency, with a sign inversion. It is due to the fact that an increase of refractivity leads to an increase of phase, but it is defined negative, so an increase of phase means the phase becoming more negative.

Numerically, (4.4) compares the values of APS and the values of atmospheric phase in the points where the stations are located, by considering them vectors. In this way, the coefficient obtained is 0.565, corresponding to an angle between
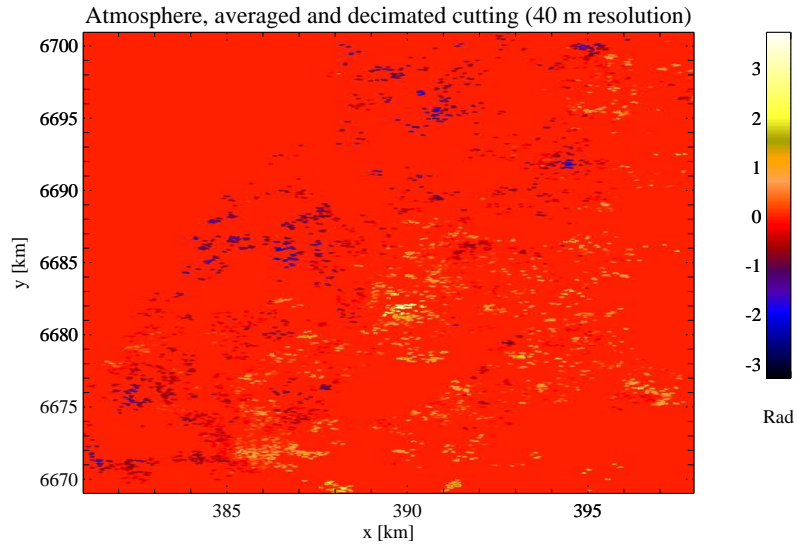
Figure 5.1: Atmospheric residue of the interferogram corresponding to the dates 2006-07-25 and 2006-08-29. It has a resolution of 40 m, so as to observe its points more clearly. It is a cutting of the complete residue, to represent the same area then the cutting of the APS.

Figure 5.2: APS of the instants 2006-07-25/09h30m00s and 2006-08-29/09h30m00s. Only the positions of the stations of the HTB (and the pixels surrounding it) displays a value. There are 13 stations.

both vectors of 55.6°. There are 13 stations in the region where the coefficient is calculated, so the vectors have 13 positions.

The coefficient associated to gaussian random vectors, of 13 elements, is 0.277. It is a 50 % lower than the real coefficient, so, in conclusion, there is a certain similarity between the i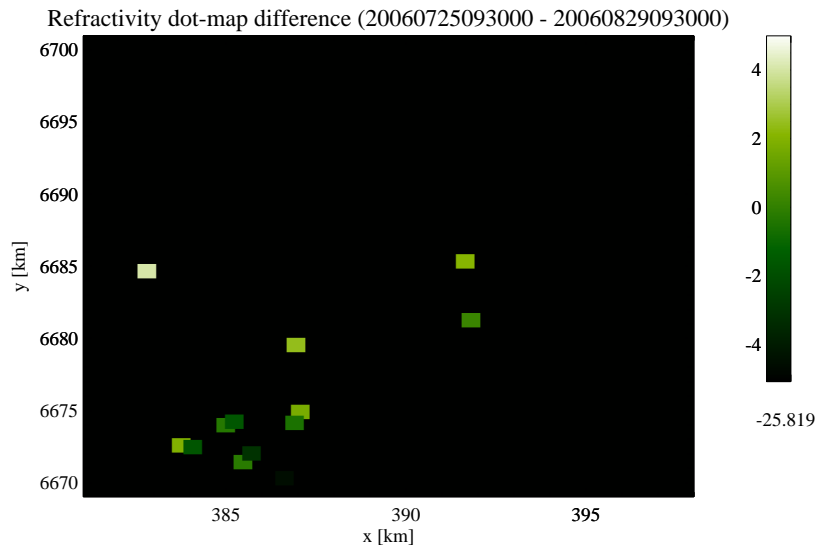nterferometric atmospheric residue of phase and the difference of values of refractivity calculated in the ground. Nonetheless, there is only one studied case, because of the problem of mismatch between the available interferograms and the data of the Helsinki Testbed. To validate the results, a study with more comparisons than just one must be done.

5.3 Results of the atmospheric spatial behaviour processing

This section deals with the presentation of the results obtained from the processing of Section 4.4, the value of the correlation distance of the atmosphere. The input data is a set of residual phases, owing to the atmospheric component. It is interesting to contrast the spatial behaviour of the atmosphere of Helsinki and Barcelona, because they are zones with a very different climate.

5.3.1 Results in Barcelona

The total of atmospheric phase residue matrixes of Barcelona is 49, one for each SLC.

Table 5.1 shows the correlation distance for each season, as well as the generic value, called the annual value. The generic value is 2.54 km, a figure that is pretty superior to the standardised value of 1 km. The values of correlation distance in a specific season are of the order of the generic value, except for Winter, when the correlation distance is 0.9 km above the generic value.

Figure 5.3 represents the distance of correlation versus the date of acquisition, while Figure 5.4 displays the distances of correlation sorted per months. In this way, seasonal or annual trends can be obtained (a distance of correlation value of 0 in the figures means that the distance could not be calculated).

The maximum value of the autocorrelation matrix is also worth studying. It is related to the variation of phase. More variation will lead to a higher mean power. Figure 5.5 shows the the mean power values versus month and day of acquisition of Barcelona.

Table 5.1: Atmospheric distance of correlation of each time of the year in the area of Barcelona.

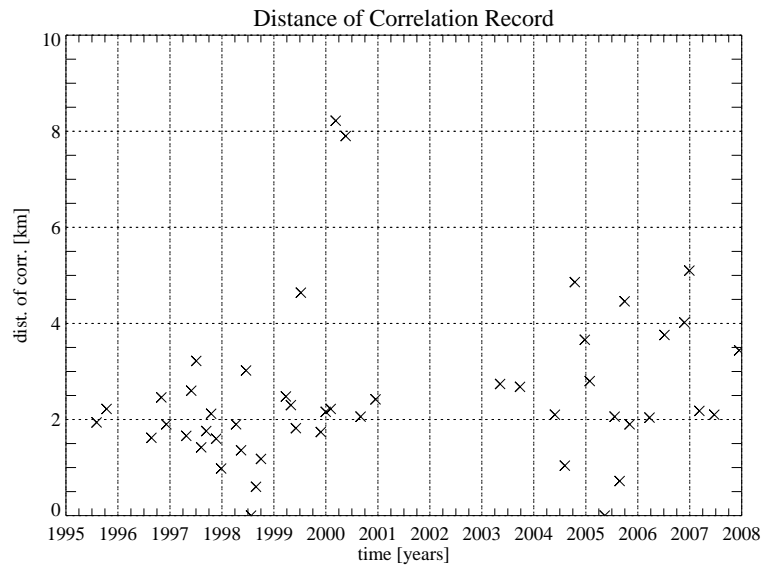| Season	Corr. distance [km]	N. of elements
Annual	2.54	49
Winter	3.44	8
Spring	2.44	13
Summer	2.54	14
Autumn	2.52	14

Figure 5.3: Distance of correlation of Barcelona versus date of acquisition
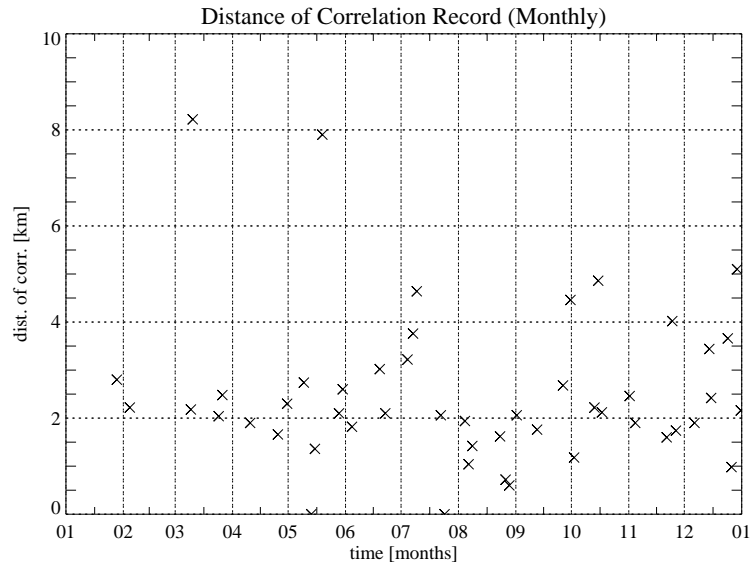
Figure 5.4: Distance of correlation of Barcelona versus month and day of acquisition
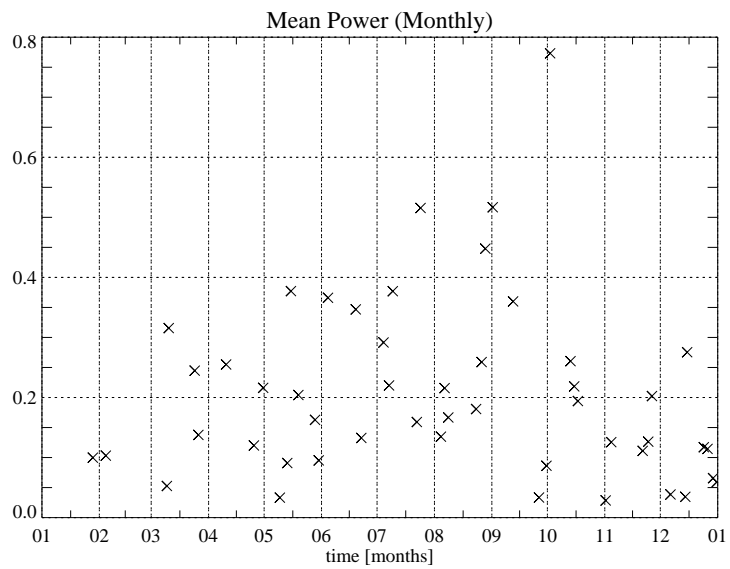

Figure 5.5: Mean power of the residue matrix of Barcelona, versus month and day of acquisition

Table 5.2: Distance of correlation of the atmosphere of each time of the year in the zone of Helsinki

Season	Corr. distance [km]	N. of elements
Annual	1.04	12
Winter	1.00	3
Spring	1.16	5
Summer	0.98	4
Autumn	-	0

5.3.2   Results in Helsinki

The distance of correlation is also calculated for the set of residues of Helsinki. The number of SLCs available of Helsinki is, however, 12, which is a very low figure.

Table 5.2 displays the atmospheric correlation distance for each season and the generic or annual value. This generic value is 1.04 km, but this figure has not the contribution of the whole year, because there are no images from Autumn. Thus, the seasonal distance of correlation gains importance. These values are of the order of 1 km, and concretely, the value in Summer is 0.98 km, below 1 km.

The representation of distance of correlation versus the date of acquisition is shown in Figure 5.6, and Figure 5.7 displays the distances of correlation sorted per months. A distance of correlation equal to 0 in the figures means that the distance could not be calculated. This is critical in the case of Helsinki, due to the low number of SLCs. Therefore, the actual number of elements in the average autocorrelation of Winter is 2, instead of 3.

5.3.3   Discussion

The value of atmospheric distance of correlation of Barcelona is 2.54 km. It is so superior to the standard value, 1 km, that does not present any problem, since the spatial filtering with a window size of 1 km continues being valid to filter matrixes whose distance of correlation is bigger.

The spatial behaviour of the atmosphere in Spring, Summer and Autumn is very similar to the annual behaviour, so is the characteristics of the atmosphere. In Winter the distance of correlation is a 35.4 % superior to the annual value. As a hypothesis, this value could mean that, in this period, the atmosphere is calmer than the rest of the year, that is, variations of the spatial distribution of the atmosphere in Winter are lower. In contrast, the planetary boundary layer in
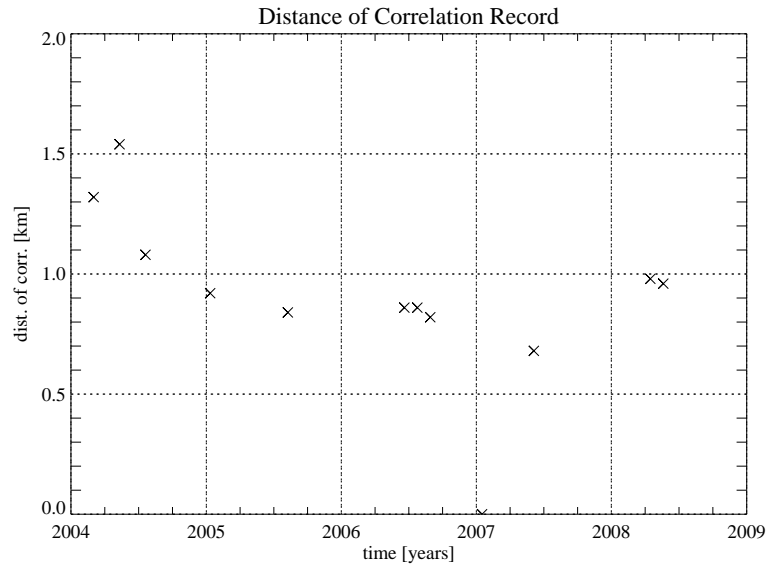
Figure 5.6: Atmospheric distance of correlation of the area of Helsinki versus date of acquisition
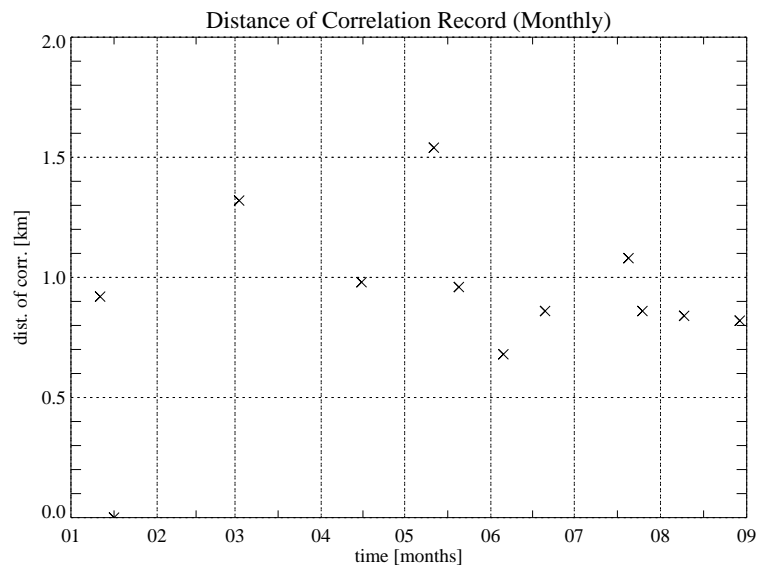

Figure 5.7: Atmospheric distance of correlation of the area of Helsinki versus month and day of acquisition

cold season tends to be thinner, leading to higher variations in the atmospheric spatial distribution. This difference implies that in the studied cases the dominant fluctuations are not tropospheric.

Figure 5.4 shows that there is a quite stable tendency independently of the month, despite some elevated values of correlation distance in July, October and December. In Figure 5.5, Summer months have a higher mean power. It could mean that in this season the variation of phase is higher than in other seasons, as expected, because in warm season the atmospheric circulation is higher.

In Helsinki, the results are quite different. However, these results are incomplete because of the low number of SLCs. The seasonal distances of correlation are around 1 km. Concretely, the value in Summer is 0.98 km, below 1 km, but the difference is minimum to consider that a spatial filtering will negatively affect the interferometric phase.

It is interesting to contrast Helsinki with Barcelona, because they are zones with a very different climate conditions. It is clear that there is a difference in their distances of correlations. The one of Helsinki is lower than that of Barcelona, so it means that the water vapour distribution is more homogeneous in Barcelona. The comparison, because of the lack of SLCs of Helsinki, is not accurate.

Chapter 6

Conclusions and future research lines

This project is a research on the relationship between the atmosphere and SAR interferometry, and presents two main results.

First, it studies the relations between the APS in InSAR and ground-based measurements of refractivity. However, the available data is insufficient (specifically, the number of SLCs of Helsinki is low) to extract conclusions. This work presents the basis to study the relationship, but it should be extended by doing the comparisons with a large data set.

It could be interesting to monitorise the variations of refractivity by means of the atmospheric component of interferometric phase and to compare them with measurements of systems that observe water vapour variations, as refractivity depends on water vapour.

The second result is the calculation of the atmospheric distance of correlation in the APS. The standard figure that is used in interferometric processing is 1 km. It is lower than or similar to the values of the distance of correlation of Barcelona and Helsinki, so the spatial filtering does not eliminate useful information. However, the separation of the atmospheric phase and the non-linear phase could be improved by using a specific parameter for the zone of study. Calculations of the value for other geographic zones will enable to know whether the standard value of the correlation distance is suitable for any set of interferograms.

As an extension of the project, it could also be useful to study the type of filter that best separates the atmospheric phase and the non-linear deformation phase.

Finally, the evaluation of the DInSAR product (the velocity of surface deformation) calculated with specific distance of correlation should be compared with the velocity of deformation obtained with the classical processing.

Bibliography

[1] R.F. Hansen, *Radar interferometry. Data interpretation and error analysis - Chapter 6. Atmospheric monitoring*. Kluwer Academic Publishers, 2001.

[2] R.F. Hansen, *Atmospheric heterogeneities in ERS Tandem SAR Interferometry*. Delft Univ. Press, 1998.

[3] R. Castro, *Estimacin de fenmenos atmosfricos SAR para la obtencin de medidas de deformacin de la tierra*. PFC, ETSETB, UPC, 2003.

[4] J.C. Curlander, R. N. McDonough, *Synthetic Aperture Radar*. John Wiley & Sons, 1991.

[5] M. Bará, Ll. Sagués, *Percepció remota amb el Radar d'Obertura Sintètica (SAR)*. TSC, ETSETB, UPC, 1997.

[6] C. Elachi, *Spaceborne Radar Remote Sensing Applications and Techniques*. New York Institute of Electrical and Electronics, 1988.

[7] O. Agustí, *Geocodificación directa para la generación precisa de modelos de elevación del terreno sobre áreas extensas en interferometría SAR*. PFC, ETSETB, UPC 1999.

[8] A. Arnaud et al., *ASAR ERS Interferometric Phase Continuity*. Proc. IGARSS 2003, July, 2003.

[9] D. Carrasco, *Interferometry for Digital Elevation Model Generation and Differential applications*. PhD Thesis, UPC, 1998.

[10] A. Monti Guarnieri, C. Prati, *ERS-ENVISAT Combination for Interferometry and Super-resolution*. Proc. ERS-ENVISAT Symposium 2000, October, 2000.

[11] G. Schreier, *SAR Geocoding: Data and Systems*. Wichmann, 1993.

[12] F. J. Tena, *Interferometría diferencial orientada al estudio de movimientos del suelo y propagación atmosférica a partir de imágenes SAR ERS-1/2*. PFC, ETSETB, UPC, 1998.

[13] C. Prati, F. Rocca, A. Monti Guarnieri, P. Pasquali, *Final report on ERS-1 SAR interferometric techniques and application.* ESA Study Contract Reporte, June 1994.

[14] M. Bará, *Processador multilook dimatges SAR.* PFC, ETSETB, UPC, 1996.

[15] C. López, *Multidimensional Speckle Noise. Modelling and Filtering Related to SAR Data.* PhD Thesis, UPC, 2003.

[16] F. Gatelli et al., *The Wavenumber Shift in SAR Interferometry.* IEEE Trans. On Geoscience and Remote Sensing, vol. 32, no. 4, July 2004.

[17] B. Delaunay, *Sur la sphere vide.* Bulletin of Academy of Sciences of the USSR, pp. 793-800, 1934.

[18] A. Ferretti, C. Prati, and F. Rocca, *Nonlinear subsidence rate estimation using permanent scatterers in SAR interferometry.* IEEE Trans. On Geosc. And Remote Sensing, vol. 38no. 5, pp. 2202-2212, September 2000.

[19] O. Mora, *Advanced Differential Interferometric SAR techniques for detection of terrain and building displacements.* PhD Thesis, UPC. Barcelona, 2004.

[20] S. Usai, *A Least-Squares Approach for Long-Term Monitoring of Deformations with Differential SAR Interferometry.* Proc. IGARSS 2002, Vol. 2, pp. 1247-1250, Toronto (Canada), June 2002.

[21] V. Pérez, *Estimación de la deformación no lineal del terreno mediante datos SAR adquiridos por satélite.* PFC, ETSETB, UPC, 2002.

[22] D. Navarrete, *Interferometría diferencial SAR con imágenes de los satélites ERS y ENVISAT.* PFC, ETSETB, UPC, 2004.